Title

Modeling of Topological States of Matter: Gate Controlled Majorana Fermions and Transport Signature of Antiferromagnetic Skyrmions

Author

Djavid, Nima

Publication Date

2019

Peer reviewed|Thesis/dissertation

UNIVERSITY OF CALIFORNIA
RIVERSIDE

Modeling of Topological States of Matter: Gate Controlled Majorana Fermions and Transport Signature of Antiferromagnetic Skyrmions

A Dissertation submitted in partial satisfaction
of the requirements for the degree of

Doctor of Philosophy

in

Electrical Engineering

by

Nima Djavid

December 2019

Dissertation Committee:

Dr. Roger K. Lake, Chairperson
Dr. Xi Chen
Dr. Peng Wei

The Dissertation of Nima Djavid is approved:

Committee Chairperson

University of California, Riverside

Acknowledgments

I would like to express my gratitude and appreciation to my supervisor Roger Lake for teaching everything I know about quantum transport and device modeling. Without his constant guidance, this work would not be possible. I would also like to thank my lab-mates for their friendship and support. I acknowledge the activities of student community of Iran at UCR through which I found a living Iran around myself. I would like to thank my family for supporting me to pursue my dreams. Within all of their limitations they provided me with the best. Special thanks to Dr. Gen Yin from UCLA which helped me to improve my coding skills, and numerical modeling.

The text of this dissertation, in part or in full, is a reprint of the material as it appears in the following journals and/or proceedings: Applied Physics Letters [1], Reprinted with permission from [1], [2018], American Institute of Physics. The co-author Roger K. Lake, listed in the above publications directed and supervised the research which forms the basis for this dissertation.

The work described in Chapters 2 and 3 was supported by the National Science Foundation under Award NSF EFRI-1433395 2-DARE: Novel Switching Phenomena in Atomic Heterostructures for Multifunctional Applications and in part by FAME, one of six centers of STARnet, a Semiconductor Research Corporation program sponsored by MARCO and DARPA. The work described in Chapter 4 was supported in part by the Spins and Heat in Nanoscale Electronic Systems (SHINES) an Energy Frontier Research Center funded by the U.S. Department of Energy, Office of Science, Basic Energy Sciences under Award #DE-SC0012670.

To my parents for all the support.

ABSTRACT OF THE DISSERTATION

Modeling of Topological States of Matter: Gate Controlled Majorana Fermions and Transport Signature of Antiferromagnetic Skyrmions

by

Nima Djavid

Doctor of Philosophy, Graduate Program in Electrical Engineering
University of California, Riverside, December 2019
Dr. Roger K. Lake, Chairperson

Half-integer conductance, the signature of Majorana edge modes, was recently observed in a thin-film magnetic topological insulator / superconductor bilayer. Chapter 2 of this thesis analyzes a scheme for gate control of Majorana zero modes in such systems. Gating the top surface of the thin-film magnetic topological insulator controls the topological phase in the region underneath the gate. The voltage of the transition depends on the gate width, and narrower gates require larger voltages. Relatively long gates are required, on the order of 2 μm, to prevent hybridization of the end modes and to allow the creation of Majorana zero modes at low gate voltages. Applying voltage to T-shaped and I-shaped gates localizes the Majorana zero modes at their ends. This scheme may provide a facile method for implementing quantum gates for topological quantum computing.

The extremely small energy splitting of Majorana zero modes caused by s-wave pairing makes identifying them experimentally very challenging. A heterostructure between a magnetic TI and a high Tc superconductor, which has an order of magnitude enhancement in the induced pairing gap, may offer a more feasible approach. In Chapter 3, we study

the effect of top surface electrical gating on a TI / high-Tc-superconductor with $d_{x^2-y^2}$ pairing. We calculated the phase diagram using the Kubo formula to find the required condition for the topological superconductivity Chern number ±1, which is necessary for obtaining Majorana modes. We show that chiral Majorana modes appear by applying the gating potential to the top surface of the TI. We also show that we are able to change their propagation direction by only changing the top gating potential. In the end, we apply the gating potential locally to create localized Majorana zero modes. Although bound states appear at zero energy, and they are robust against an increasing gating potential, we find that the wave functions of these zero energy modes do not fulfill the wavefunction condition of a Majorana zero mode, namely that a Majorana mode is its own anti-particle.

In Chapter 4, the effect of an antiferromagnetic Skyrmion on the tunneling magnetoresistance of a ferromagnet/insulator/antiferromagnet/ferromagnet heterostructure is numerically investigated. The tunneling magnetoresistance in the presence of a Bloch type antiferromagnetic Skyrmion is significantly reduced when the polarization of the ferromagnetic leads is anti-parallel. The amplitude of the output signal, caused by the transmission of current in the presence of Skyrmion, depends on the resistance change induced by the Skyrmion. The change in the resistance can be engineered by changing the thickness of the insulator and magnetization strength of the ferromagnetic leads. This scheme can be used for electrical detection, and the read-out of antiferromagnetic Skyrmions in the future of Skyrmion based antiferromagnetic memories.

Contents

List of Figures

Chapter 1

Rationale

1.1 Introduction

Topologically protected material systems are highly robust against small changes in system parameters and can not be disturbed by local perturbations. This property is very useful for applications in the field of quantum computing and antiferromagnetic Skyrmion based memory [2]. Materials showing topologically protected quasiparticles, and those exhibiting topologically non-trivial spin textures, have motivated many studies on new energy-efficient spintronic devices and topological qubits [3–5].

Majorana fermions are among the topologically protected quasiparticles that are predicted to be a key element in the topological quantum computing [6]. Ettore Majorana first introduced them to theoretical physics [7]. Majorana fermions are particles that, unlike electrons and positrons, constitute their own antiparticles. In operator language, it is reflected as $\Psi^\dagger = \Psi$. Although they have been elusive in high energy particle physics, it is predicted that they can emerge as non-trivial excitations in hybrid solid-state materials [8].

Superconductors in which fermions pair are ideal structures for hosting such quasiparticle excitations. The quasiparticle excitation in superconductors is a superposition of electrons and holes, and they are called Cooper-pairs. In s-wave pairing, the superconductivity arises from electron-hole pairs carrying opposite spins. The quasiparticle operator can be written as $z = uc_{\uparrow}^{\dagger} + vc_{\downarrow}$ which is distinct from $z^{\dagger} = u^{*}c_{\uparrow} + v^{*}c_{\downarrow}^{\dagger}$. Therefore, the spin singlet pairing prevents the s-wave superconducting state from satisfying the condition $\Psi^{\dagger} = \Psi$.

As a result, superconductors with spinless pairing provide an ideal platform for Majorana fermions. Spinless pairing occurs in p-wave superconductivity with $p + ip$ pairing in two dimensions. These superconductors support exotic excitations in their boundaries and topological defects [9, 10]. Localized modes that form at the ends of a 1D topological p-wave superconductor [9], and that bind to vortices of $p + ip$ superconductors are the most important examples [11]. p-wave superconductors are extremely rare in nature, and they exhibit low superconductivity correlation in comparison to the long-range assumption in the Kitaev model.

Most proposals for engineering a 1D Kitaev model exploit a proximity effect to a s-wave superconductor. Spin-orbit coupling, in conjunction with time-reversal symmetry breaking, can effectively convert such a system to a p-wave superconductor.

1.2 Motivation

1.2.1 Majorana fermions

Fu and Kane's proposal [8], for generating Majorana fermions at the edges of a topological insulator (TI) in the proximity of an *s*-wave superconductor, was breakthrough in this field. Numerous studies were conducted to find a signature of Majorana fermions in this platform. In 2015 a theoretical study on transport signature of chiral Majorana edge modes showed that a half-integer conductance plateau in a topological-insulator/superconductor/topological-insulator is a signature of a Majorana edge mode [12]. This signature was experimentally observed in a magnetic topological insulator/superconductor heterostructure [13]. They observed this phenomenon in a $\mathrm{Bi_2Se_3}$ thin film in proximity to Nb, which is an *s*-wave superconductor. This finding inspired the idea of designing a new platform based on the same material for the creation and braiding of Majorana zero modes described in Chapter 2. However, a small pairing gap is a problem that makes the detection of Majorana modes much harder. New materials with proximity induced high-Tc superconductivity have been proposed. It is claimed that cuprates can induce large *s*-wave and *d*-wave pairing simultaneously in $\mathrm{Bi_2Se_3}$ [14]. Therefore, in Chapter 3, we explore the possibility of having Majorana modes and the necessary condition for their creation in a TI/d-wave superconductor system.

1.2.2 Antiferromagnetic Skyrmions

Over the last few years, antiferromagnetic spintronics has received significant attention from the magnetism community, as antiferromagnetic materials have several inherent properties that could lead to better spin dynamic performance suitable for practical applications [15]. In very recent years, theoretical studies have suggested that antiferromagnetic Skyrmions may have higher velocity compared to their magnetic counterparts [16].

The Magnus force in current-driven magnetic skyrmions causes an undesired transverse shift, which results in the destruction of skyrmion at sample edges. In ferromagnets, the magnetic skyrmion is driven by an external force, such as the spin current, that usually shows an undesired transverse velocity, which may result in the destruction of the skyrmion at the sample edges. In antiferromagnetic materials, skyrmions are regarded as two coupled magnetic skyrmions with opposite topological charges. Since the total topological number of an antiferromagnetic skyrmion is zero, the Magnus force is eliminated, leading to the straight motion of skyrmions along the force direction. More theoretical works also predict that skyrmions in synthetic antiferromagnets made from stacking ferromagnetic skyrmions in opposite directions are also immune to the Magnus effect [17]. New experimental work shows that skyrmions can be stabilized at room temperature in synthetic antiferromagnets [18]. Based on these promising recent results, we investigate a new scheme for the electrical detection and read-out of skyrmions in antiferromagnets. Vertical detection is compatible with conventional electronic technology and easy to engineer. Our goal is to study the tunneling magnetoresistance of antiferromagnetic skyrmions to find their signature in the magneto resistance.

Chapter 2

Gate Controlled Majorana Zero Modes on a Two-Dimensional Topological Superconductor

2.1 Introduction

Majorana fermions are charge-neutral fermionic particles that are their own antiparticles originally proposed by Ettore Majorana [7]. Prior theoretical work suggested that Majorana fermions could exist in topological superconductors as elementary excitations [19–22]. The first experimental demonstration was the zero-bias anomaly observed in a III-V semiconductor nanowire coupled to an s-wave superconductor [23, 24], a material system that is a physical implementation of Kitaev's one dimensional topological superconductor model [19]. In the middle of the superconducting gap, zero-energy localized states appear at the ends of such nanowires. These states are Majorana zero modes (MZMs). MZMs obey non-Abelian statistics, [25] and they can be used for fault-tolerant, topological quantum computing [26, 27]. This requires the precise control of the position of the MZMs in a nanowire network. Gate control has been proposed and analyzed [27, 28], and recent experiments demonstrated prototypes of such nanowire networks [29].

Although previous experiments using III-V nano-wires have shown exciting possibilities, an implementation in two-dimensional (2D) thin films would be more compatible with conventional semiconductor device fabrication. Such a scheme in the InAs / superconducting system has been proposed [30]. Recently, quantized half–integer conductance ($\frac{e^2}{2h}$) was observed in a different material system consisting of a thin film magnetic topological insulator (MTI) capped by an s–wave superconductor (Nb) [31]. The half–integer conductance suggested the existance of a chiral Majorana mode propagating along the edge [31–34]. In this system, the MTI consisted of Cr doped, epitaxial, thin film $(\mathrm{Bi,Sb})_2\mathrm{Te}_3$. Recently, signatures of MZMs were observed in a similar material system by scanning probe measurements, where the anti-periodic boundary condition is induced by a superconducting vortex [35]. Prior theoretical studies on the MTI–superconductor system focused on the topological phase diagram [36], and the most recent theoretical studies propose gate control of MZMs in ribbon geometries with large aspect ratios [37, 38].

In this study, we build upon that recent work. We theoretically demonstrate the micron–scale gate dimensions required for creating MZMs, and we analyze how gate geometry effects the gate voltage required to create the MZMs. The system under consideration is an array of ‘keyboard’ gates [37] on top of the MTI / superconductor bilayer as illustrated in Fig. 2.1. The effect of the geometric shape of the gated area on unwanted hybridization and the topological band gap is analyzed. Fundamental building blocks of the crossbar gate-array, the I-shaped and the T-shaped gates, are demonstrated. To ensure that the MZMs are not trivial low energy modes, the symmetry of the MZM wave functions are analyzed to show that the the wave function is its own complex conjugate.

2.2 Hamiltonian

The system, as shown in Fig. 2.1, consists of a thin-film MTI placed on the top of an s-wave superconductor. Electric gates on top of the MTI control the top-surface electrostatic potential. The Hamiltonian of the system is [39]

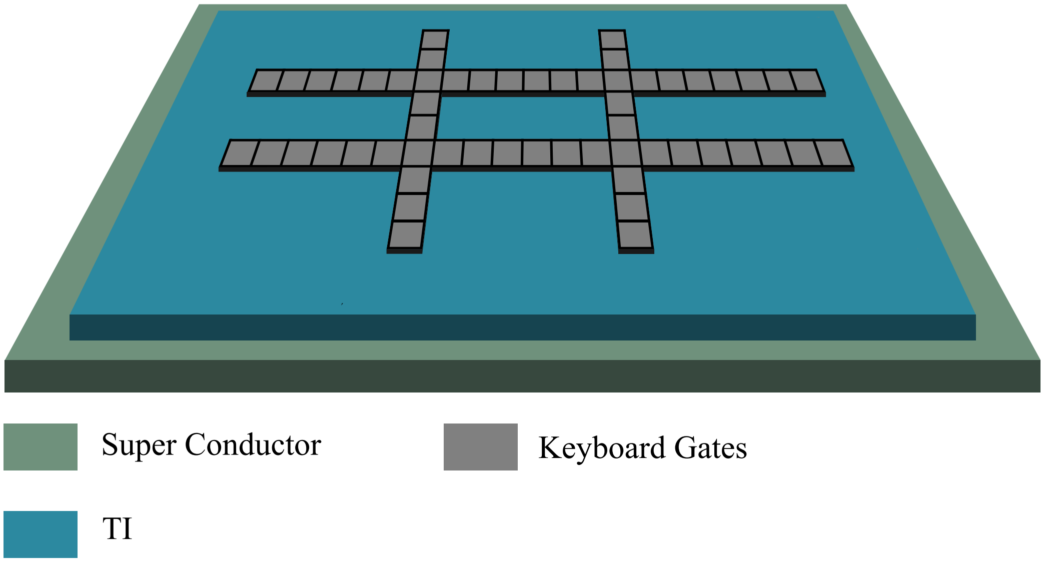

Figure 2.1: A quantum anomalous Hall insulator/ superconductor heterostructure. The crossbar shaped gates at the top, can change the electro-static potential of the top surface locally.

$$H_{BdG} = \begin{pmatrix} H_0(k) - \mu & \Delta_k \\ \Delta_k^\dagger & -H_0^*(-k) + \mu, \end{pmatrix}. \tag{2.1}$$

where

$$\Delta_k = \begin{pmatrix} i\Delta_t \sigma_y & 0 \\ 0 & i\Delta_b \sigma_y \end{pmatrix}, \tag{2.2}$$

and

$$H_0(k) = \hbar v_f(k_y\sigma_x - k_x\sigma_y)\tilde{\tau_z} + m(k)\tilde{\tau_x} + J_H\sigma_z + \frac{V_g}{2}(\tilde{\tau_z} + I). \tag{2.3}$$

$\Psi = [(\psi_{\uparrow t}\ \psi_{\downarrow t}\ \psi_{\uparrow b}\ \psi_{\downarrow b}),\ (\psi^\dagger_{\uparrow t}\ \psi^\dagger_{\downarrow t}\ \psi^\dagger_{\uparrow b}\ \psi^\dagger_{\downarrow b})]$ is the basis of the Hamiltonian where $\psi_{\uparrow t}(k)$ corresponds to an up-spin electron on the top surface and $\psi^\dagger_{\downarrow b}(k)$ corresponds to a down-spin hole at the bottom. $\boldsymbol{\sigma}$ and $\tilde{\boldsymbol{\tau}}$ are Pauli matrices corresponding to the spin and the top-bottom surfaces, respectively. Δ_t and Δ_b are the proximity-induced Cooper-pairing interactions at the top and bottom surfaces, respectively. The pairing interaction of the bottom surface that is in contact with the superconductor is $\Delta_b = 1.4$ meV [40], and at the top surface, $\Delta_t = 0$. $m(k) = m_0 + m_1k^2$ represent the hybridization of the top and bottom surfaces of the thin–film MTI. The value of these terms for 3 quintuple layers of $\mathrm{Bi_2Se_3}$ are $m_0 = 138$ meV and $m_1 = 18$ eVÅ^2 [41, 42]. The quantity $\hbar v_F = 3.29$ eVÅ is consistent with DFT results [43]. J_H is the Hund's rule coupling from the ferromagnetic exchange interaction induced by the Cr dopants. For calculations using a fixed J_H, the value is $J_H = 130$ meV. The chemical potential $\mu = 0$. The last term in Eq. (2.3) represents the gate voltage V_g applied at the top surface of the MTI, with the bottom surface adjacent to the superconductor at ground. An equivalent approach would be to shift μ by $-V_g/2$ in Eq. (2.1) and apply the gate voltage symmetrically across the top and bottom layers such that the bottom layer is shifted to $-V_g/2$ and the top layer is shifted to $+V_g/2$. This latter approach is the way the gate voltage was included in recent work [37].

2.3 Numerical modeling and results

2.3.1 Phase diagram and Majorana chiral modes

To model finite and spatially varying structures, the Hamiltonian is transformed into a tight–binding model on a square lattice by substituting $k_x \to -i\frac{\partial}{\partial x}$ and $k_y \to -i\frac{\partial}{\partial y}$ in Eq. (2.1) and discretizing the derivatives using a 1 nm discretization length [44]. Each site in the tight-binding model is then represented by an 8×8 matrix corresponding to Eq. (2.1) with the inter–site matrix elements coming from the discretized derivatives. Eigenenergies and eigenstates of the discretized, spatially–varying systems are calculated numerically using a Lanczos algorithm. The eigenstate calculations use periodic boundary conditions, and the simulation domain is sufficiently large that the gated regions in the neighboring cells do not interact with each other. Simulation domains are illustrated in Figs. 2.3(a,b) and 2.4(a,b).

For the calculation of conductance shown in Fig. 2.2(d), the transmission is determined in the usual way from the 'device' Green's function and the lead self-energies [45]. In the calculation of the lead self energies, an imaginary potential $-i\eta$ with $\eta = 0.1$ meV is placed on the diagonal of the discretized H_{BdG} to assist convergence of the surface Green's function. The zero–temperature, two–terminal conductance is then $\sigma_{xx} = \frac{e^2}{h}T(E_F)$ where $T(E_F)$ is the transmission coefficient at the Fermi energy.

To investigate a single edge mode of a semi-infinite plane ($-\infty < x \leq 0$ and $-\infty < y < \infty$) as shown in Fig. 2.2(b,c), only the substitution $k_x \rightarrow -i\frac{\partial}{\partial x}$ is made, and the derivative is discretized on the 1 nm grid. Since the edge of the half-plane is parallel to $\hat{y}$, k_y remains a good quantum number. The Hamiltonian then becomes a semi-infinite, one-dimensional chain model, where each site of the chain is represented by a 8×8 k_y–dependent matrix. The 8×8 edge Green's function $G^R(k_y, E)$ is calculated using the decimation method [46,47]. Note that this is traditionally referred to as the 'surface Green's function,' however, for this system, the 'surface' is an 'edge.' To resolve the edge spectrum, the energy broadening η used in the calculation of the surface Green's function is 1 meV, which is chosen to be five times larger than the energy discretization step size. The spectral function at the edge site is $A(k_y, E) = -2\,\mathrm{Im}\left\{\mathrm{tr}\left[G^R\left(k_y, E\right)\right]\right\}$.

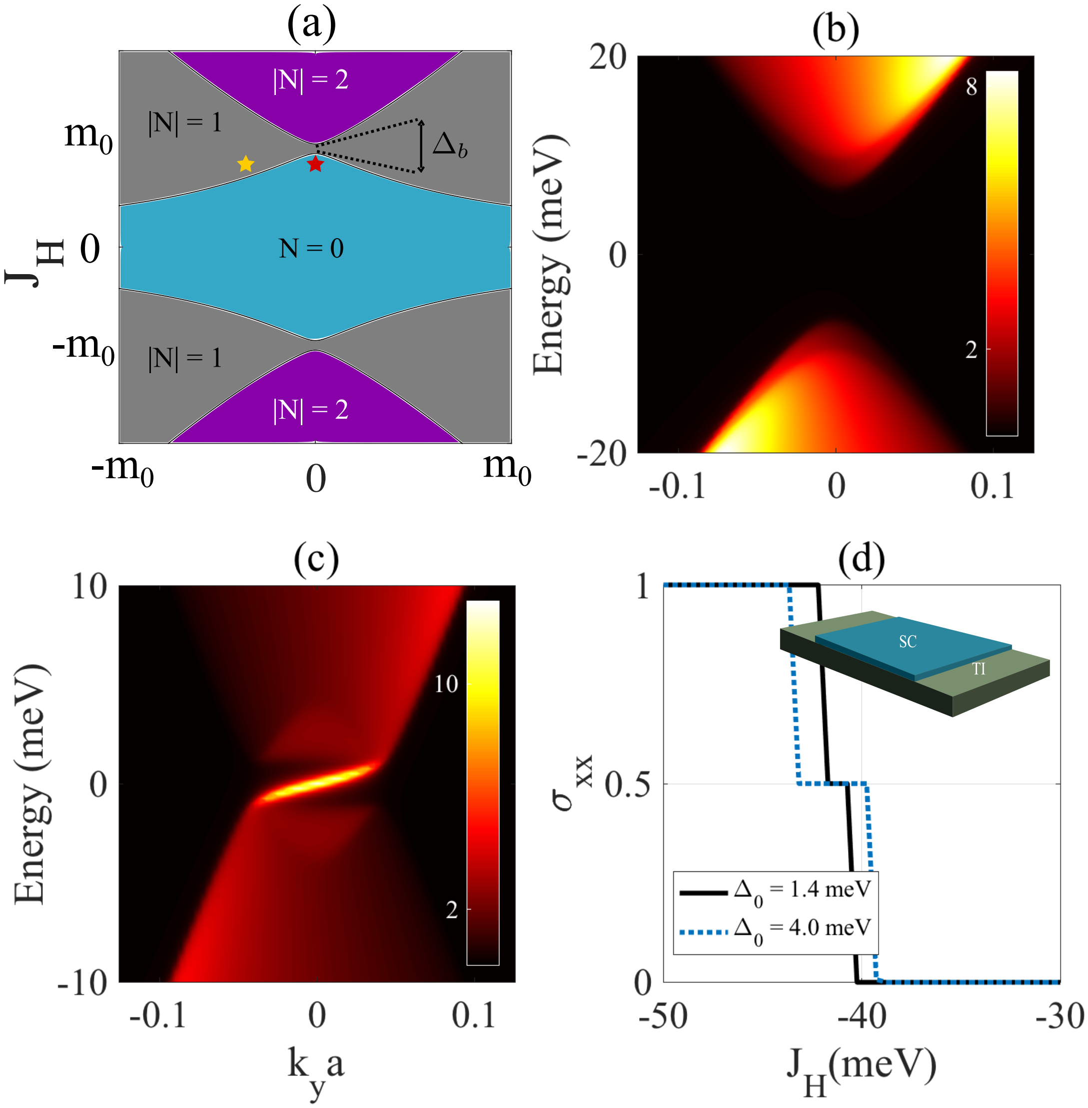

Figure 2.2: (a) Phase diagram of the system with $\Delta_t = 0$. V_g is applied to the top surface. (b) and (c) show the spectral function $A(k_y, E)$ at the edge site ($x = 0$) of a semi–infinite plane ($-\infty < x \leq 0$ and $-\infty < y < \infty$) at different gate voltages. (b) V_g = 0.0 mV corresponding to the red star in (a) and (c) V_g = -30 mV corresponding to the yellow star in (a). (d) The half-integer plateau in conductivity of a 100 nm wide by 40 nm long MTI / superconductor bilayer with topological insulator leads for two different values of Δ_t as shown in the legend. E_f = 0.1 meV, V_g = 0, and Δ_b = 0. Inset: Illustration of the structure.

In the superconducting Nambu space, the topological superconducting Chern number (TSC), N, is allowed to be $-2, -1, 0, 1, 2$ where N characterizes the number of chiral edge modes [33]. One practical way to tune the TSC number is to apply an out-of-plane external electric field to modify the top-surface electrostatic potential energy [33, 37]. The topological phase diagram of the system represented by Eq. (2.1) is plotted in Fig. 2.2(a) as a function of the top-gate potential V_g and the magnitude of the exchange energy J_H. The phase boundaries are obtained by the gap closing in the BdG Hamiltonian (Eq. (2.1)) at $k = 0$. To determine the the TSC number in each region, we evaluate the number of edge states from the bandstructure calculation of a 150 nm wide ribbon that is periodic along x. N is the number of the degeneracy of the edge states along one edge. The ribbon width is chosen to be sufficiently wide such that the hybridization of the edge states is negligible. The blue area belongs to the trivial phase ($N = 0$) of a normal insulator. The purple regions correspond to $N = 2$, which is topologically equivalent to a non-superconducting quantum anomalous Hall insulator with Chern number $C = 1$. In the grey areas, $N = 1$, and a single Majorana edge mode propagates along the edges. As shown in Fig. 2.2(a), when V_g is zero, $N = 1$ only occurs over a narrow range of exchange potentials. Therefore, gating the top surface can control the transition between different topological phases.

To demonstrate the voltage-controlled topological transition, we numerically calculate the edge-state spectrum of the semi-infinite plane at different values of V_g. A semi-infinite plane is chosen to ensure that the edge state hybridization is zero since the opposite edge is at $x = -\infty$. Choosing the parameters for $N = 0$ and $N = 1$ as shown by the two points in Fig. 2.2(a), the edge spectral function is plotted versus k_y and E in Figs. 2.2(b) and (c), respectively. In Fig. 2.2(b) the applied voltage is zero, $N = 0$, and a trivial gap opens at the Dirac point. Applying a $-30\,\mathrm{mV}$ potential to the top surface, a topological transition occurs, and a gapless Majorana edge mode appears as shown in Fig. 2.2(c).

For further verification of the model, we construct a 2-terminal, finite-width device consisting of a central superconducting / MTI bilayer region with two non-superconducting, topological insulator leads mimicking the experimental setup recently reported [33]. The structure is illustrated in the inset of Fig. 2.2(d) where the length of the superconductor area is 40 nm and the width is 100 nm. As seen in Fig. 2.2(d), a half-integer plateau in conductivity appears during a scan of the Hund's-rule exchange energy J_H, which emulates a scan of an externally applied magnetic field. This plateau is the result of a combination of normal reflection and Andreev reflection [33].

2.3.2 Majorana zero modes

We now show that a voltage applied to a gate with a large aspect ratio can create localized Majorana zero modes at the ends. Fig. 2.3 shows the simulation geometry that consists of a long, thin, gated region within a rectangular supercell. The dimensions of the gated region are 28 nm $\times$ 1.8 μm, and the dimensions of the supercell are 100 nm $\times$ 2 μm. Fig. 2.3(a) is a color map of of the lowest positive–energy ($E \geq 0$) state $|\psi_i|^2$ at each site i at a gate voltage of $V_g = -30$ mV. The thin width of the gated area, 28 nm, is less than the penatration depth of a Majorana edge mode. This hybridizes the states on the opposing long edges of the gated region, so that a gap is opened in the energy spectrum and there is no zero–energy mode along the edges. Further decreasing V_g to -55 mV, a pair of bound states appear at the ends of the gate as shown in Fig. 2.3(b), and the energy of these bound states drops 15 to 16 order of magnitude from 7 meV to $\sim 10^{-15}$ meV, suggesting that they are MZMs. The hybridization of the MZMs at the ends of the gated regions is negligible since they are 1.8 μm apart. When the gate length is reduced to 1.3 μm, hybridization is no longer negligible, the energy always remains numerically finite, and it reaches a minimum value of 6×10^{-6} meV.

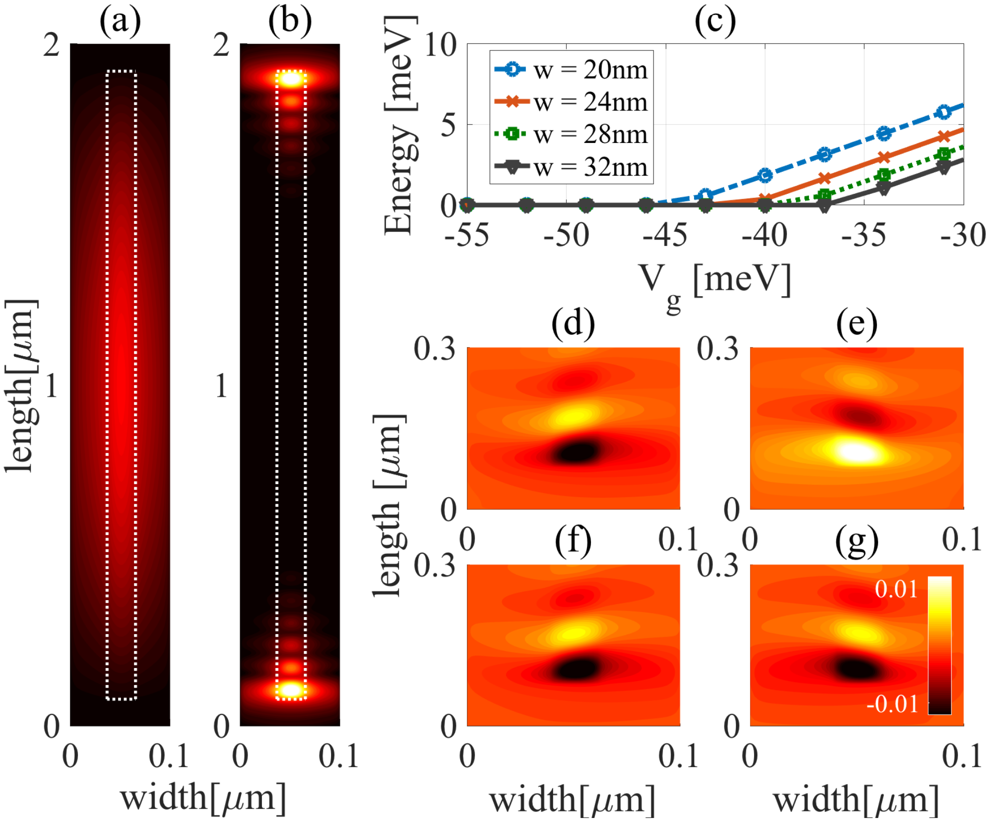

Figure 2.3: (a) The lowest positive–energy state at $V_g = -30$ mV. It transitions into (b) two MZMs at $V_g = -55$ mV. (c) Ground state energy as a function of the applied voltage for different widths. The length is fixed at 1.8 μm. Components of the MZM used to verify that the zero–energy mode is indeed a Majorana mode: (d) $\text{Re}[\langle\gamma|\psi_{\uparrow b}\rangle]$ (e) $\text{Im}[\langle\gamma|\psi_{\uparrow b}\rangle]$ (f)$\text{Re}[\langle\gamma|\psi^{\dagger}_{\uparrow b}\rangle]$ (g) $\text{Im}[\langle\gamma|\psi^{\dagger}_{\uparrow b}\rangle]$

The voltage at which the topological transition occurs depends on the geometry of the gated region. Fig. 2.3(c) shows a calculation of the ground state energy as a function of the gate voltage for 4 different gate widths. The gate lengths are fixed at 1.8 μm. For each gate width, there is a critical gate voltage at which the ground-state energy goes to zero. The required magnitude of V_g to achieve the zero-energy state increases as the gate width decreases.

To confirm that the localized end-modes are indeed MZMs and not simply very low-energy states, the eigenvectors Ψ of the zero-modes are analyzed to determine if they satisfy the property $\Psi = \Psi^\dagger$. The eight coefficients of each mode at each site j can be divided into four groups with each of the groups containing a pair of coefficients that are complex-conjugate, as shown in Eq. (2.4).

$$\begin{aligned}\Psi =& A(1-i)\psi_{\uparrow_t} + A(1+i)\psi^\dagger_{\uparrow_t} \\ &+ A(1-i)\psi_{\uparrow_b} + A(1+i)\psi^\dagger_{\uparrow_b} \\ &+ B(-1+i)\psi_{\downarrow_t} + B(-1-i)\psi^\dagger_{\downarrow_t} \\ &+ B(1-i)\psi_{\downarrow_b} + B(1+i)\psi^\dagger_{\downarrow_b}\end{aligned} \tag{2.4}$$

Ψ is the wave function of a MZM, and A, B are the site–dependent normalization coefficients. The real and imaginary parts of $\langle\Psi\,|\psi_{\uparrow b}\rangle$ and $\langle\Psi\,\left|\psi^\dagger_{\uparrow b}\right\rangle$ are shown in Fig. 2.3(d)-(g). Numerically, $\mathrm{Re}[\langle\Psi|\psi_{\uparrow b}\rangle]$ and $\mathrm{Re}[\langle\Psi|\psi^\dagger_{\uparrow b}\rangle]$ are identical, whereas $\mathrm{Im}[\langle\Psi|\psi_{\uparrow b}\rangle]$ and $\mathrm{Im}[\langle\Psi|\psi^\dagger_{\uparrow b}\rangle]$ have different signs, which satisfies Eq. (2.4). Similar results are obtained for the other bases. This confirms that the zero–energy states are MZMs.

2.3.3 Braiding Majorana zero modes

The motivation for an array of crossbar gates is to mimic a 1D network of wires for gate–controlled transfer and exchange of MZMs. A fundamental building block of such a network is a T–junction as shown in Fig. 2.4. With voltage applied to the vertical section of the gate, two MZMs are created at the ends of the I-shaped gated area. Turning off the voltage of the lower gate and applying it to the horizontal gate results in the MZM at the end of the 'L'. The MZM does not appear at the sharp corner of the 'L'. Controlling the voltages of the gates moves the topological regions ($N = 1$) and the associated MZMs. Such a network of top gates can implement a pixel-by-pixel control of the geometric shape of the topological region, such that more complicated braiding operations can be achieved within this scheme.

All of the calculations presented are for 3 quintuple layers. In terms of the model Hamiltonian (2.3), only the interlayer hybridization terms, m_0 and m_1, change due to layer thickness. For example, at 5 quintuple layers, their values become $m_0 = 41$ meV and $m_1 = 5$ eVÅ^2 [42]. The phase diagram of the topological transitions shown in Fig. 2.2(a) does not change. This means that the optimum value for $|J_H|$ is approximately m_0.

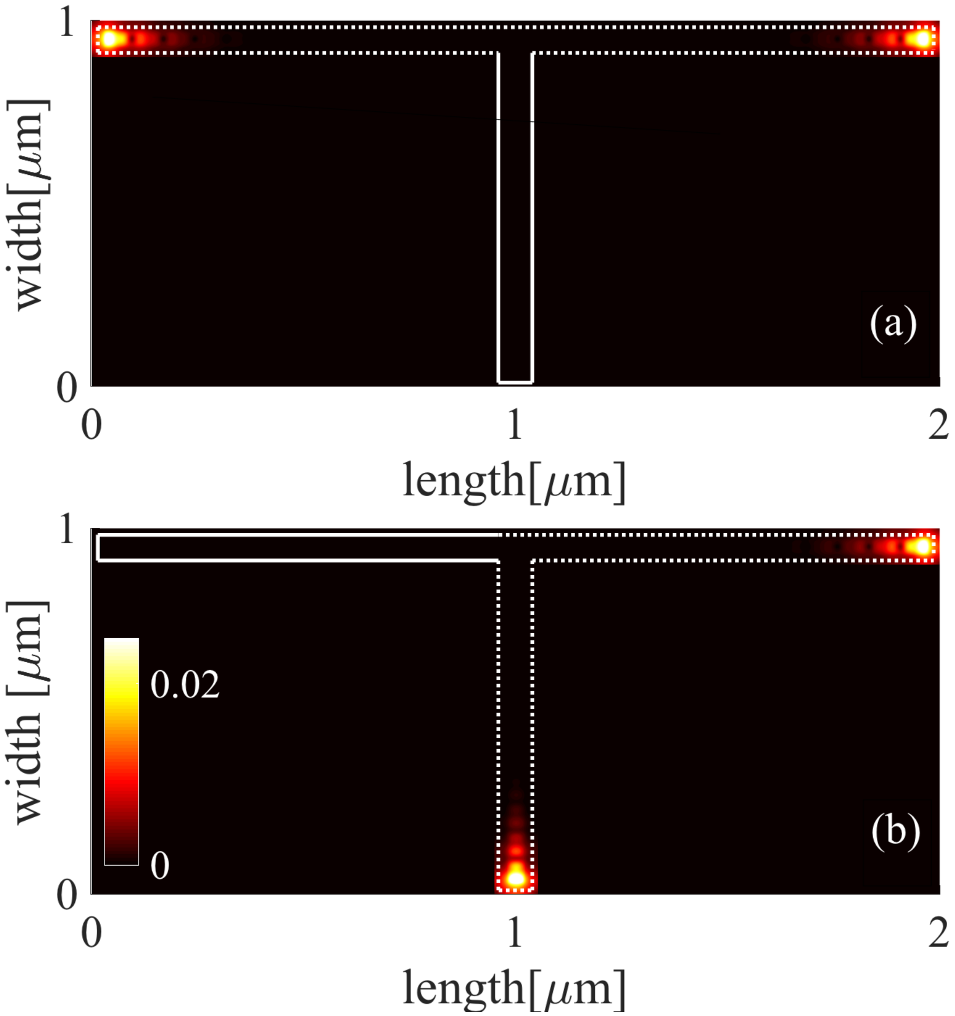

Figure 2.4: Shifting the MZM in the left (a) to the bottom (b) by changing the gate electric potential. The gates are set to be on and off inside the dashed and solid lines, respectively. The widths of the gated regions are 70nm.

In other words the spin-splitting due to the magnetic exchange interaction from the Cr dopants should be close to the hybridization gap induced by the inter-surface coupling of the top and bottom layers. Also, the gate voltage scales as m_0. Thus, smaller inter-surface coupling allows lower voltage operation.

However, the values of m_0 and J_H affect the energy, temperature, and length scales. The MZMs of interest live within the spin and hybridization energy gap. As J_H and m_0 are reduced, lower temperatures would be required to prevent population of the excited states and maintain the magnetic ordering. The hybridization gap $2m_0$ affects the spatial extent of the MZM wavefunctions. As this energy gap shrinks, the spatial extent of the MZM wavefunction increases, and this increases the inter-edge tunneling. The increased tunneling necessitates both wider and longer gate regions to keep the required applied voltage $V_g < m_0$. Thus, thicker films with lower inter-surface hybridization require smaller exchange coupling, and allow lower voltage operation, but at the cost of lower temperatures and larger areas.

2.4 Conclusion

In summary, a gated MTI / superconductor bilayer provides a platform for 2D spatial control of Majorana zero modes. The phase diagram of the system shows that a gate voltage can control the topological transition between the $N = 0$ and $N = 1$ states. The voltage of the transition depends on the gate width, and narrower gates require larger voltages. Relatively long gates are required, approximately 2 μm, to prevent hybridization of the end modes and to allow the creation of MZMs at low gate voltages. The MZM positions are controlled by the local gating of the top surface. Sequential clocking of an array of gates provides a method of braiding MZMs.

Chapter 3

Electrically induced quasi-particle bound states in high T_c topological superconductors with $d_{x^2-y^2}$ pairing

3.1 Introduction

Majorana edge modes were detected by observation of half-integer conductivity in a magnetic topological insulator/superconductor (MTI/SC) heterostructure [31]. Recently proposed systems that are compatible with standard semiconductor processing are the most promising schemes for braiding Majorana modes. However, definite proof of Majorana zero modes has been lacking, and identifying them experimentally has been challenging mostly because of the small pairing gap of s-wave SCs. A heterostructure between an anomalous quantum insulator and a high Tc d-wave superconductor with a large pairing gap may offer a more feasible approach for implementing Majorana bound states. The existence of Majorana bound states in high-T_c magnetic impurity chains [48], Majorana edge states in iron-based superconductors [49] and Majorana corner modes in a high-temperature platform [50] are some the of previous studies on the Majorana modes on High Tc superconductors. On the other hand fully gapped topological surface states in $\mathrm{Bi_2Se_3}$ can be induced by a d-wave high-temperature superconductor [14]. Also, evidence for Majorana bound states in an iron-based superconductor has been experimentally claimed [51].

In this work, we study the topological properties of a gated unconventional (MTI/SC) heterostructure. The phase diagram of the system is obtained by employing the Kubo formula. The existence of Majorana edge modes in the presence of electrical gating has been studied for the first time in d-wave topological superconductors. A Green's function formalism has been employed for the detection of Majorana edge modes, and their localization properties have been investigated.

3.2 Model

3.2.1 Hamiltonian and d-wave pairing

We start with a quantum anomalous Hall insulator (QAHI) surface states Hamiltonian:

$$H_0(k) = \hbar v_f(k_y\sigma_x - k_x\sigma_y)\tilde{\tau_z} + m(k)\tilde{\tau_x} + J_H\sigma_z + \frac{V_g}{2}(\tilde{\tau_z} + I). \tag{3.1}$$

where $\tilde{\tau}$ and σ are Pauli matrices of the top and bottom surfaces and spin, respectively. v_f is the Fermi velocity, J_H is magnetism induced by dopants, V_g is the applied electric potential to the top surface, and $m(k) = m_0 + m_1k^2$ is the hybridization between the top and bottom surfaces.

To induce superconducting gap in the surface states we insert H_0 in to the BdG hamiltonian,

$$H_{BdG} = \begin{pmatrix} H_0(k) - \mu & \Delta_k \\ \Delta_k^\dagger & -H_0^*(-k) + \mu, \end{pmatrix}. \tag{3.2}$$

with

$$\Delta_k = \begin{pmatrix} i\Delta_t\sigma_y & 0 \\ 0 & i\Delta_b\sigma_y \end{pmatrix}, \tag{3.3}$$

$\Delta_{t,b}$ are the top and bottom surface pairing gaps. The superconductor is at the bottom surface, so $\Delta_t = 0$. For high Tc cuprates the gap function is

$$\Delta(\mathbf{k}) = \Delta_0(\cos k_x - \cos k_y) \tag{3.4}$$

for $d_{x^2-y^2}$ pairing [50].

Fig. 3.1 shows the bandstructure resulting from Eq. (3.2) with $d_{x^2-y^2}$ pairing. The corresponding top gating potential of the red curve is 50 meV, and the dotted blue line is 100 meV. When the applied potential is zero, the system is gapless and has a trivial phase. By increasing the applied voltage, the gap is closed at the Γ point and continues to move away from the Γ point as the voltage is increased. Therefore the system is in a non-trivial topological phase.

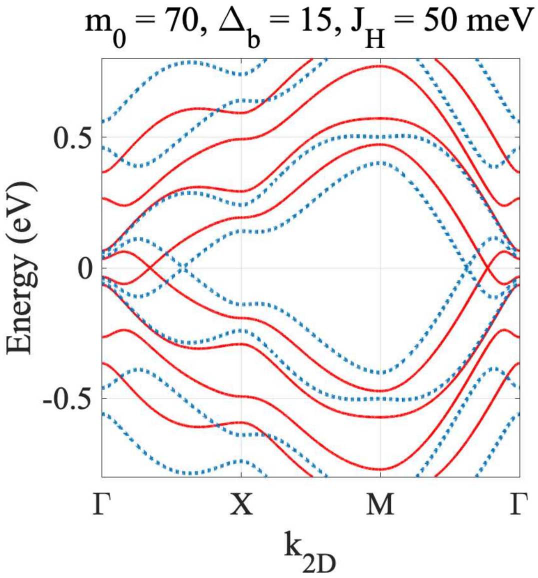

Figure 3.1: Bandstructure of a topological d-wave superconductor. Red-curves and black curves correspond to $V_g = 50$ meV and $V_g = 100$ meV, respectively. The gap is closed at the Γ point, and by increasing the applied voltage, it moves away from the Γ point.

3.2.2 Analytical phase diagrams

To find the phase diagram, we diagonalize the Hamiltonian at the Γ point. The eight energy levels obtained from diagonalizing the Hamiltonian at $\mathbf{k} = 0$ are given by Eq. (3.5).

$$E = \pm(\frac{Vg}{2} - \mu \pm J_H) \pm \frac{\sqrt{V_g^2 + 4m_0^2}}{2} \tag{3.5}$$

By setting $E = 0$, we find the boundaries at which the trivial gap closes and re-opens. These are the boundaries between the different topological regions. Two variables that govern the bandstructure are V_g and J_H. Therefore we plot a 2D phase diagram in which these two parameters are the corresponding axes. By plotting the obtained lines, the phase diagram is separated into eight regions. To find the topological superconducting Chern number of the system of each region, we choose a set of points within the region, and we find the number of edge states from the transmission or from a wide ribbon band structure calculation. From Eq. (3.4), we see that the value of the pairing gap is zero at the Γ point. Therefore, the phase diagram is general for any d-wave pairing with zero pairing potential at the Γ point.

The resulting phase diagrams are shown in Fig. 3.2. Fig. 3.2(a) is the phase diagram of a topological superconductor for $\mu = 0$. As we see for $V_g = 0$, there is a direct transition from the trivial gap to $N = \pm 2$, which is the topological superconductivity Chern number of the system. To have the topological condition for hosting Majorana modes, the topological Chern number of the system must be $N = \pm 1$. In Fig. 3.2(b), μ is set to be non-zero. In this condition, we can get $N = \pm 1$ without applying the gate potential. Figs. 3.2(c, d) are the phase diagrams for $|J_H| = |m_0|$ and $|J_H| < |m_0|$, respectively. The green area corresponds to $N = 1$. By applying the values chosen from the phase diagram to the whole top surface, a Majorana mode appears at each edge of our system.

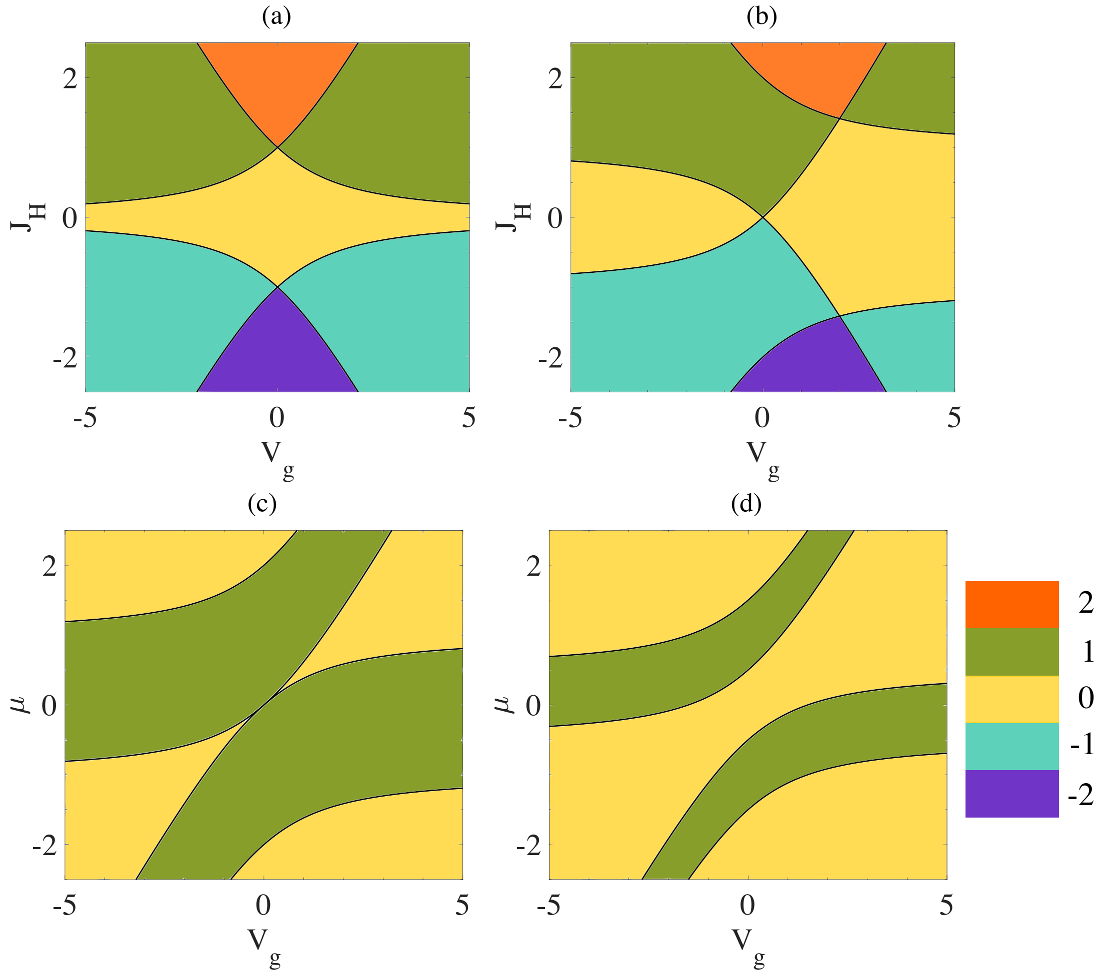

Figure 3.2: (a)Phase diagram of the system for $\mu = 0$. For $V_g = 0$, N goes directly from zero to two. (b) $\mu = |m_0|$ (c) $|J_H| = |m_0|$ and $|J_H| < |m_0|$. All the numbers are in the units of $|m_0|$.

3.2.3 Kubo formula and Numerical phase diagrams

In this section, we use a different approach to determine the phase diagram and topological superconducting Chern number of the system. We employ Kubo formula to calculate the Chern number of the system. According to Kubo formula the Hall conductance is [52]

$$\sigma_{xy} = -\frac{ie^2}{h}\frac{2\pi}{L^2}\sum_{n,k} f(E_{nk}) \times \sum_{m(\neq n)} \frac{\left\langle nk|\frac{\partial H}{\partial k_x}|mk\right\rangle \left\langle mk|\frac{\partial H}{\partial k_y}|nk\right\rangle - (n \leftrightarrow m)}{(E_{nk}-E_{mk})^2}, \tag{3.6}$$

where $\sum\limits_{m(\neq n)}$ is the summation over the bands, and $f(E)$ is the Fermi distribution function. We can rewrite the Kubo formula at zero temperature as $\sigma_{xy} = \frac{e^2}{h}\sum_{n:\text{filled}} N_n$ where N_n is the Chern number of the nth band. The total topological superconductor (TSC) Chern number of the system is $N = \sum_{n:\text{filled}} N_n$. To verify the phase diagrams in the previous section, we calculate the phase diagram for $\mu = 0$ and $\mu = m_0$.

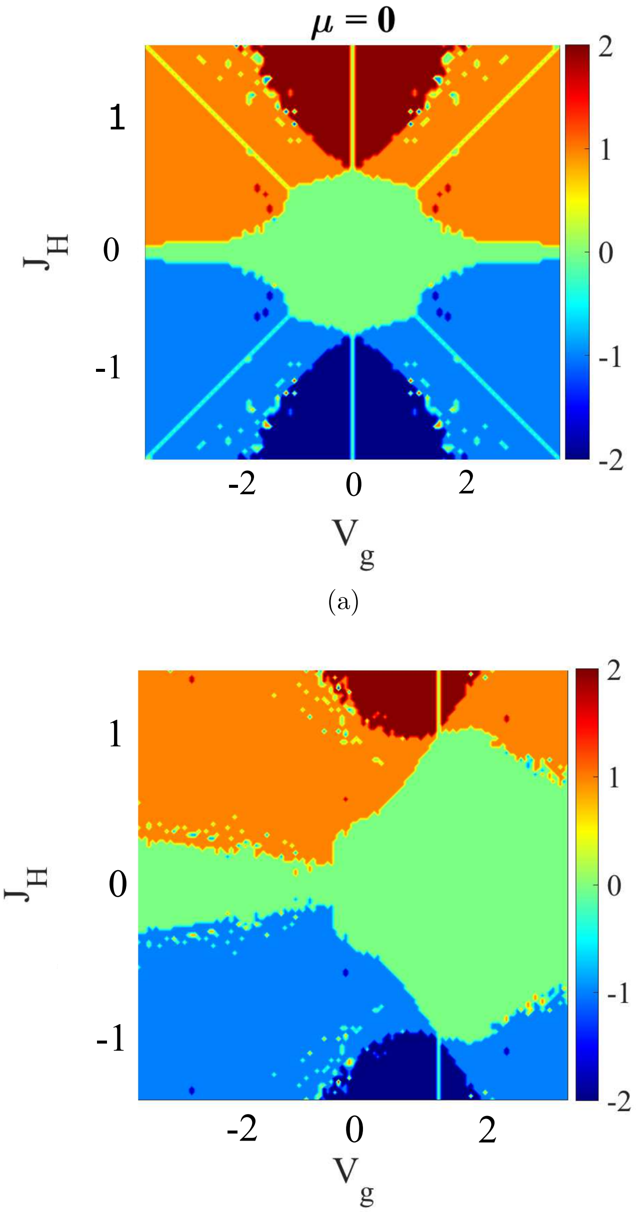

(a)

(b)

Figure 3.3: Phase digram of a d-wave topological superconductor for (a) $\mu = 0$ and (b) $\mu = m_0$. All the numbers are in the unit of m_0. The phase diagrams are obtained from the Kubo formula. The colorbar is the topological Chern number of the system (N).

Comparing Fig. 3.3 with Fig. 3.2 verifies the phase diagram obtained from analytical calculations. The orange and cornflower blue colors correspond to the topological superconductivity Chern number ±1 ($N = \pm 1$). For $\mu = 0$, increasing the gate potential makes it more feasible to achieve the necessary condition for hosting Majorana modes. The realistic magnitude of J_H, which comes from the magnetic doping, is still not well understood experimentally. However, In the presence of a gate potential, the range of J_H in which the Chern number remains ±1 is larger and we can choose a smaller value for the exchange potential to obtain the desired Chern number. Therefore gating the top surface is a tool to create a platform for hosting Majorana modes without having certainty on the magnitude of exchange potential induced by the Cr doping.

By using the Kubo formula, we can calculate the phase diagram for even larger gating potentials and extend our phase diagram. Fig. 3.4 is the extended Kubo phase diagram of a $d_{x^2-y^2}$ pairing high T_c topological superconductor. The sign of the Chern number indicates the propagation direction. We can see in Fig. 3.4 that, changing the amplitude of the gating potential not only can change the number of propagating edge modes, but it can also change the propagation direction of a single edge mode by going from $N = +1 \ \rightarrow N = -1$ directly.

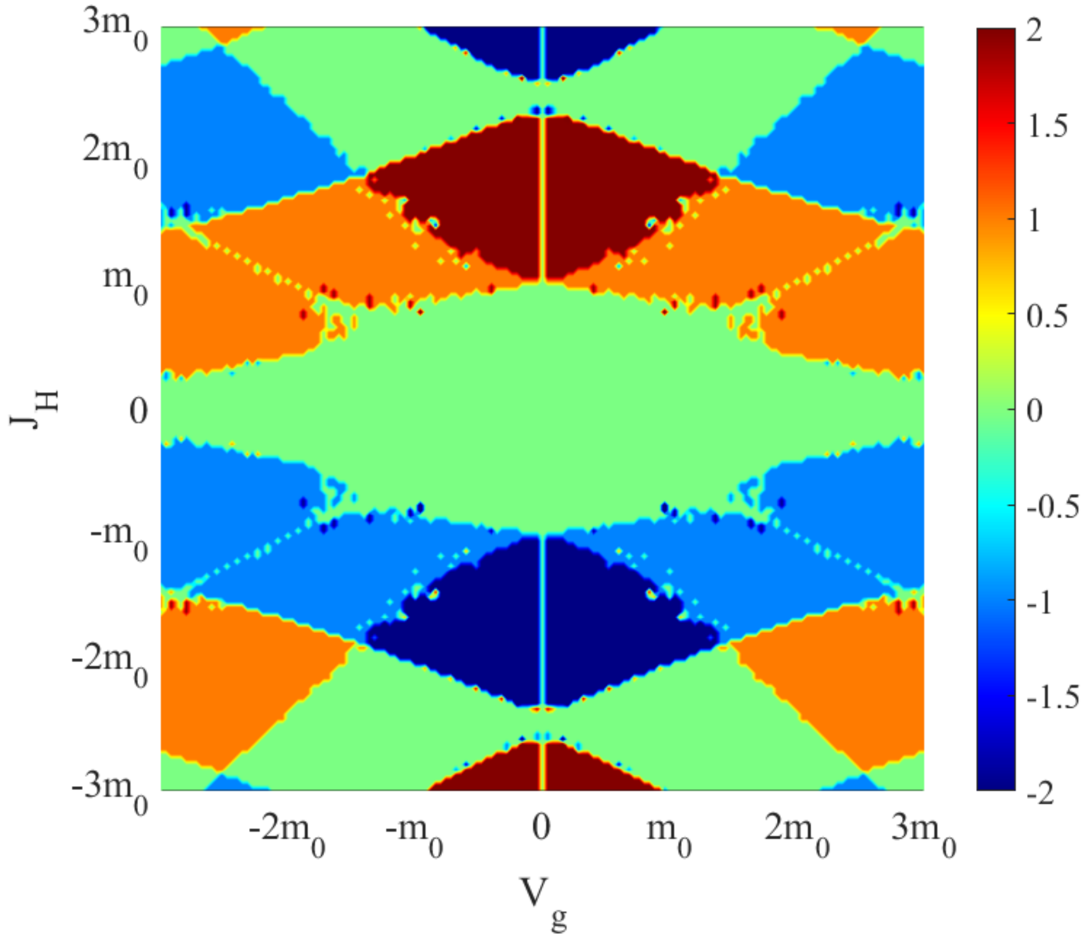

Figure 3.4: Extended d-wave pairing phase diagram obtained from the Kubo formula. The orange and cornflower colored regions correspond to $N = \pm 1$. For $N = \pm 1$, our system can harbor a single Majorana mode at domain boundaries. The color bar indicates the topological superconducting Chern number.

3.3 Majorana modes

3.3.1 Chiral Majorana edge modes

The existence of chiral Majorana modes (CMMs) in nodal superconductors has been theoretically studied [53,54], however, they have not yet been experimentally observed. In this section we investigate the existence of CMMs in the presence of the applied gating potential. We use the phase diagram we obtained in the previous section to create CMMs. To get CMMs on the edges of our system, the gap must be closed and re-opened once. Therefore, by choosing a proper set of parameters that correspond to $N = \pm 1$ the chiral modes must appear at the edge of the system.

Figs. 3.5(a,b) are the spectral functions calculated at $V_g = 0$ and $V_g = 100$ meV respectively. The surface hybridization term is $m_0 = 70$ meV, $J_H = 50$ meV and the pairing potential $\Delta_b = 15$ meV. When the applied gating potential is zero in Fig. 3.5(a), the spectral function of the system has a trivial gap. If we use the same set of parameters to plot the bandstructure of a 180 nm wide ribbon in Fig. 3.5(c), we see that the bands at the Γ point do not cross each other. However, when we apply the gating potential of $V_g = 100$ meV, the gap is closed and re-opened, Fig. 3.5(d), and a chiral Dirac edge mode appears in the edge spectral function, Fig. 3.5(b).

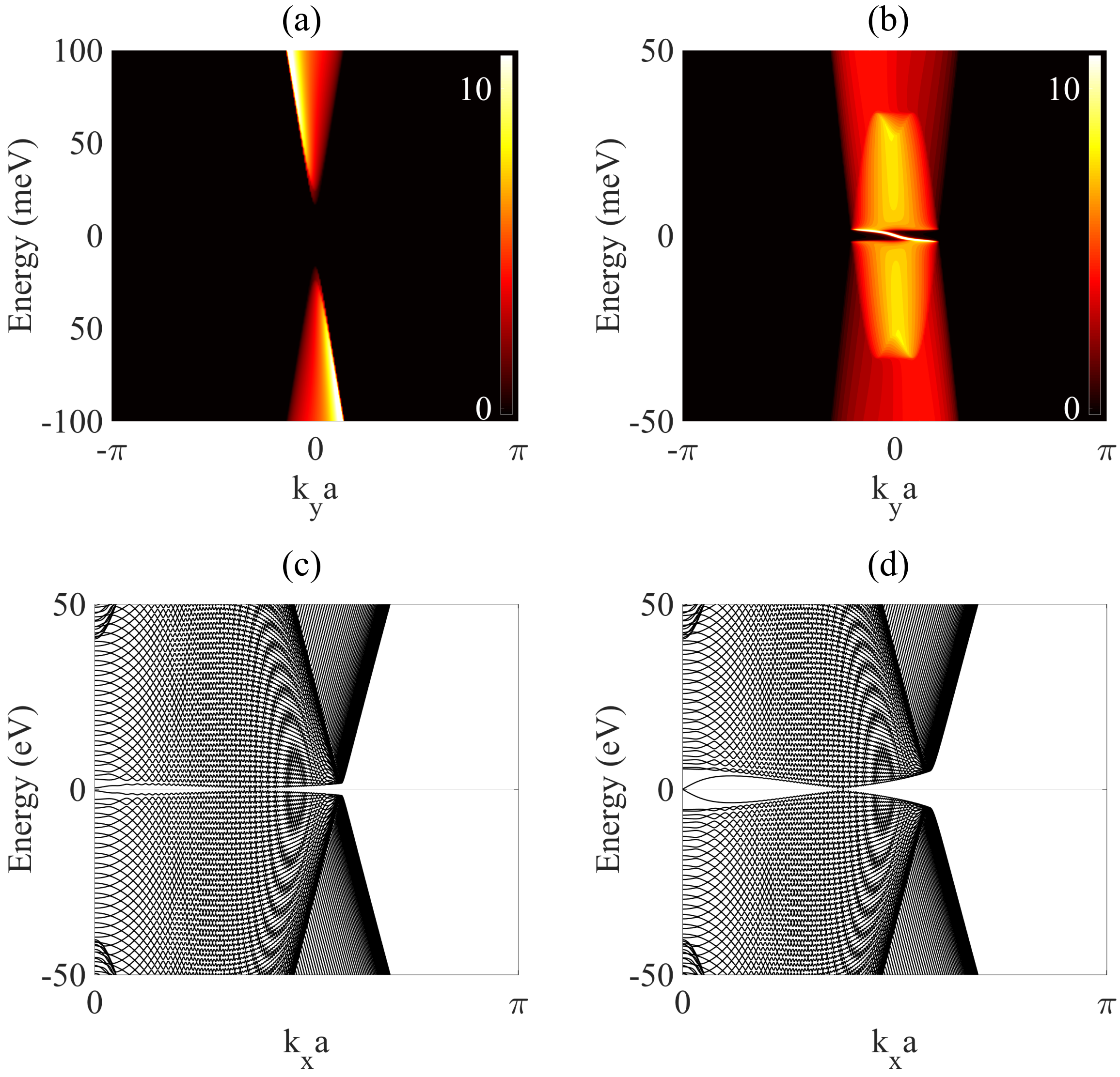

Figure 3.5: Spectral functions $A(k_y, E)$ calculated at the edge $x = 0$ of a semi-infinite ($0 \leq x < \infty$ and $-\infty < y < \infty$) topological superconductor at (a) $V_g = 0$ and (b) $V_g = 100$ meV. The corresponding bandstructures for a 180 nm wide ribbon with the same set parameters are plotted in (c) and (d) respectively. $m_0 = 70$ meV, $J_H = 50$ meV and $\Delta_b = 15$ meV.

To see if the CMMs are indeed located at the edge of the system, we plotted the local density of the states along the width of the ribbon and its corresponding band structure at $k_{2D} = 0$. Fig. 3.6(a) is the bandstructure of a 180 nm wide ribbon. For $V_g = 50$ meV, the two red bands in the bandstructure do not cross. But for $V_g = 100$ meV we can see the crossing at the Γ point. The spatial distribution of the wavefunction along the ribbon width in Fig. 3.6(b) shows that when the applied potential is zero, the wavefunction is localized in the middle of the ribbon. By increasing the applied potential, the wave function starts to move toward the edges. For $V_g = 100$ meV, the wave function is largely concentrated at the edges as we expect for chiral Majorana modes.

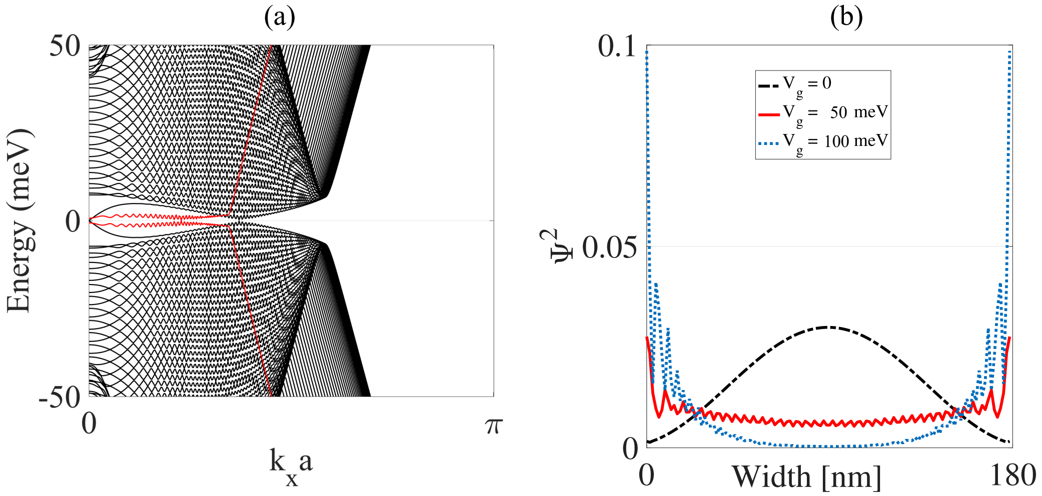

Figure 3.6: (a) Band structure of a 180 nm wide ribbon. Black curves correspond to $V_g = 100$ meV and the red curve is the lowest energy band at $V_g = 50$ meV. (b) Local density of states ($|\psi(k_x)|^2$) along the width shows how Majorana edge modes appear by increasing the electric field.

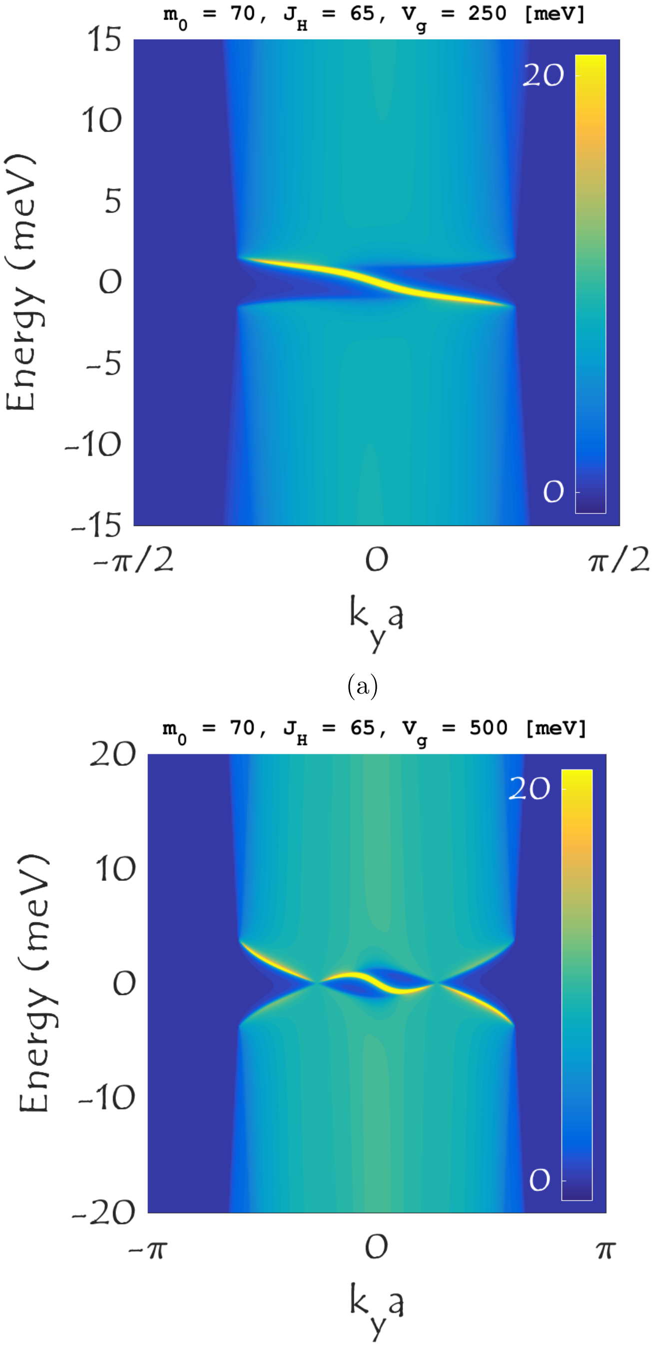

(a)

(b)

Figure 3.7: Spectral functions $A(k_y, E)$ calculated at the edge $x = 0$ of a semi-infinite ($0 \leq x < \infty$ and $-\infty < y < \infty$) at (a) $V_g = 250$ meV and at (b) $V_g = 500$ meV. Applying a large gating potential causes the balk bands touch at some k points apart from the superconducting nodal points.

Chiral Majorana modes caused by the gating potential of the top surface are robust against the increasing the applied gating potential. In Fig. 3.7, spectral functions of a semi-infinite d-wave topological superconductor plane at two different gating potentials are shown. In Fig. 3.7a, the applied potential is 250 meV, and a chiral Majorana mode at the edge of the system exists. By increasing the applied potential, as long as the topological superconducting Chern number of the system is ± 1 ($N = \pm 1$), the Majorana mode exists at the edge. In Fig. 3.7b, even by increasing the applied potential to 500 meV, the chiral Majorana mode is still at the edge. We use the same set of parameters that correspond to Fig. 3.7b and find the wave fucntion of a very wide TSC ribbon. By looking at the obtained wave function at $E = 0$ and $k_y = 0$, we confirm that it satisfies the criteria $\Psi^\dagger = \Psi$, and is, therefore, a Majorana mode.

3.3.2 Majorana zero modes

In this section, we apply the gating potential locally to the top surface of the topological superconductor with $d_{x^2-y^2}$ pairing. This applied potential creates a topological defect, and we expect to find a Majorana mode attached to these topological defects. First, we start by applying the electric potential to a long rectangle-shaped area. The width of the rectangle is 20 nm and its length is 2 nm, $J_H = 50$ meV, $m_0 = 70$ meV. Fig. 3.8 shows the density of states as a function energy, plotted for 4 different gating potentials. In Fig. 3.8(a), there are three mid-gap states at $E_1 = 2$ meV, $E_2 = 5$ meV, and $E_3 = 10$ meV. By changing the gating potential, the location of the peaks can move. In Fig. 3.8(d), when the gating potential is 80 meV, the bound state is located at zero. By increasing the gating potential further, the peak location does not change, and it is pinned at zero energy. Since Majorana bound states only appear at zero energy, we must investigate the wave-function of the zero-energy bound state to evaluate if it is indeed a Majorana zero mode. However, by evaluating the wave-function and checking for the form described by Eq. (2.4), we found that those bound states are not Majorana zero modes.

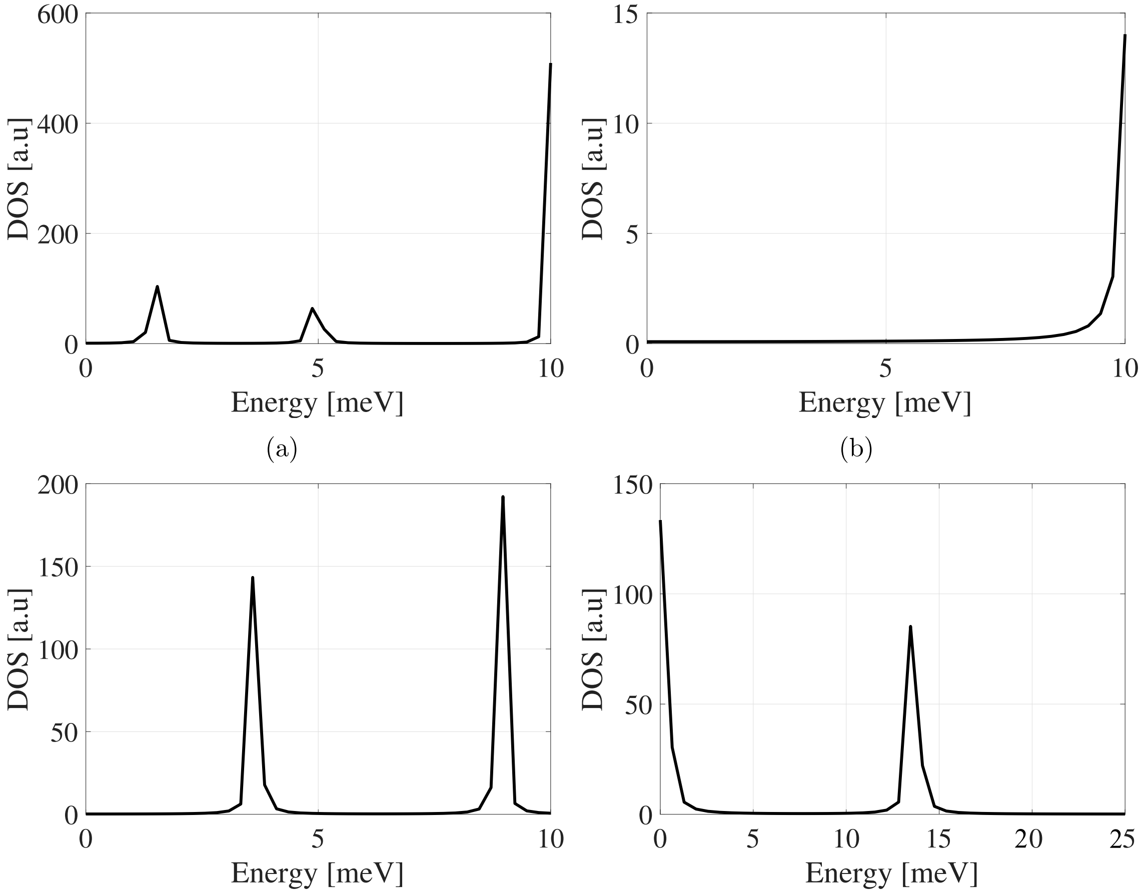

(a) (b)

(c) (d)

Figure 3.8: The density of states calculated at (a) V_g = 20 meV, (b) V_g = 40 meV, (c) V_g = 60 meV, (d) V_g = 80 meV. The peaks show the energy where the mid-gap bound states are located. The density of states is calculated by summing $|\psi^2|$ over the entire gated area.

3.4 Conclusion

In this chapter, the existence of Majorana modes in a magnetic TI in proximity to a high Tc superconductor with $d_{x^2-y^2}$ pairing has been investigated. The phase diagram of the system is obtained from the eigenvalue calculation and confirmed by using the Kubo formula. It has been shown that the required topological superconducting Chern number for having Majorana modes ($N = 1$), is achievable by gating the top surface of the magnetic TI. The top gating potential is applied to a semi-infinite 2-D plane, and a chiral Majorana edge mode appeared. We evaluated its wave function and confirmed that it is indeed a chiral Majorana mode. We applied the top surface gating potential locally in order to create localized MZMs attached at the ends of the gated area. Although localized zero-energy peaks appear in the density of states calculations which correspond to zero-energy bound states, the wavefunctions do not satisfy the criteria $\Psi^\dagger = \Psi$, and, therefore, are not Majorana zero modes.

Chapter 4

Magneto tunneling resistance of Skyrmions in layered antiferromagnetic materials

4.1 Introduction

Skyrmions are topological magnetic defects that exist in magnetic interfaces with Dzyaloshinskii-Moriya interaction [55, 56]. Since their initial discovery in B20 chiral magnets, they have been observed in a variety of materials such as Cu_2SeO_3 [57], FeGe, [58, 59] and etc. Magnetic Skyrmions (MSKX) have been the subject of intensive studies for their promising characteristics in the future memory applications. However, there are some fundamental problems with magnetic Skyrmions. Most of the proposed applications of Skyrmions in magnetic memories rely on Skyrmion propagation for data transformation. The Magnus force in current-driven magnetic Skyrmions induces a transverse movement resulting in the destruction of the Skyrmion at the sample edge. Also, the ferromagnetic order creates a dipolar field that hinders ultrasmall Skyrmion sizes.Theoretical studies, based on micromagnetic simulations, not only show that antiferromagnetic Skyrmions (ASKX) can travel in straight lines, but that they also can move faster in comparison to their ferromagnetic counterparts and can be driven with lower current densities [16,17,60]. It is also suggested that Skyrmions in synthetic antiferromagnets made from stacking ferromagnetic Skyrmions in opposite directions are also immune to the Magnus effect [17]. Also, a recent experimental work shows that ultra-small size antiferromagnetic Skyrmions can be stabilized at room temperature in Synthetic antiferromagnets [61].

Electrical detection of magnetic Skyrmions has been heavily investigated [62–66]. Among these studies, perpendicular reading of single magnetic Skyrmions in Pd/Fe/Ir(111) thin films [52], and the impact of a magnetic Skyrmion on magnetoresistance are based on vertical electron transport [67]. Due to the lack of a net magnetic moment, the detection of antiferromagnetic Skyrmion texture is very challenging [68]. Their detection method is limited to topological spin hall measurements [69] and magnetic force microscopy [61]. In this work, we study a new scheme for the detection and read-out process of layered antiferromagnetic Skyrmions (ASKX) in synthetic antiferromagnets. We calculate the tunneling magnetoresistance (TMR) of a ferromagnet/insulator/antiferromagnet/ferromagnet (FM/I/AFM/FM) heterostructure to understand how the presence of a Skyrmion influences the resistance. This scheme is simple to implement, compatible with conventional integrated circuit technology, and highly scalable.

4.2 Methodology

4.2.1 Hamiltonian

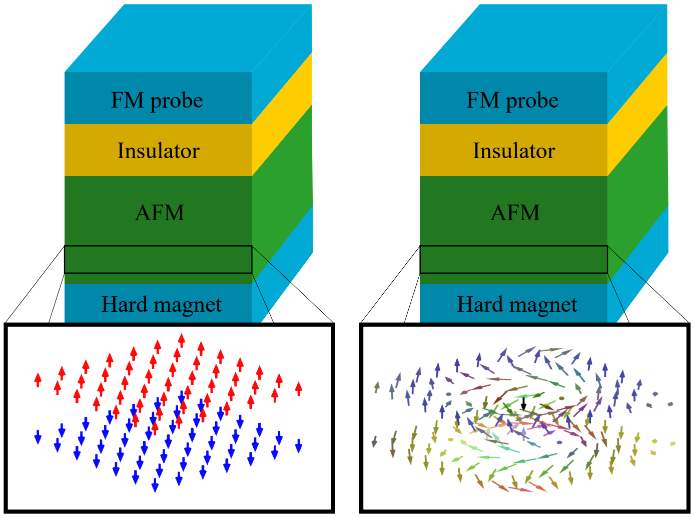

(a) (b)

Figure 4.1: A ferromagnet/ insulator/ anti-ferromagnet/ ferromagnet heterostructure with layered (a) A-type AFM, (b) AFM Skyrmion. The top ferromagnetic probe is a soft-magnet that creates a spin-polarized current with a magnetic moment in any desirable direction. The hard magnet at the bottom is a $\hat{z}$ apparatus for blocking the $S_z = +\frac{\hbar}{2}$ component of the current.

The schematic of the system is shown in Fig. 4.1. The top layer is a soft ferromagnet (SFM) in which the magnetic moment of emitted electrons is manipulated by a magnetic field. The electrons tunnel through a wide bandgap insulator (INS) to the antiferromagnet (AFM). The AFM can host a layered Bloch type antiferromagnetic Skyrmion. The bottom layer is a hard magnet (HM) and works like an apparatus for blocking a polarized current with a certain magnetic moment.

The tight-binding Hamiltonian of the system can be written as :

$$H = \sum_i c_i^\dagger m c_i + \sum_{<i,j>} (c_i^\dagger t_0 c_j + H.c.) + J_H \sum_i c_i^\dagger \sigma_i . \hat{S}_i c_i, \tag{4.1}$$

where $\hat{S}_i$ is localized spin on site **i**, t_0 is the nearest neighbor hopping term, J_H is the Heisenberg exchange potential and m is the on-site mass term.

The bandstructure of the bulk AFM, INS and FM regions are calculated as Eqs. (4.2), (4.3), (4.4), respectively. The mass term is zero in the AFM and FM region but it has a finite value inside the insulator and it's sign alternates between two adjacent insulator atomic grid points. Also, J_H is zero in the insulating region.

$$E = \pm\sqrt{J_H^2 + 2t_0^2(1 + \cos k_z a)} + 2t_0 \cos k_x a + 2t_0 \cos k_y a \tag{4.2}$$

$$E = \pm\sqrt{m^2 + 2t_0^2(1 + \cos k_z a)} + 2t_0 \cos k_x a + 2t_0 \cos k_y a \tag{4.3}$$

$$E = \pm J_H + 2t_0 \cos k_x a + 2t_0 \cos k_y a + 2t_0 \cos k_z a \tag{4.4}$$

We set $t_0 = -0.3812$ eV and m* $= 0.4m_e$ (MgO effective mass), therefore since the band dispersion is almost parabolic at the Γ point in all three band structures, the discretization length is estimated to be around 5 Å. By setting $m = 3.8$ eV the insulating gap at the Γ becomes 7.8 eV, which is the same as MgO.

Figs. 4.2a, 4.2b, and 4.2c are the ferromagnetic, antiferromagnetic and insulating band structures, respectively. Our goal is to detect the presence of Skyrmions in a layered AFM (A-type) by calculating its tunneling magnetoresistance. To inject a spin-polarized current from the soft ferromagnetic lead, we set the value of $J_{SFM} = 0.5$ eV in it. As a result, the red band is far away from the bottom of the bandstructure, and the injected current is almost %100 polarized, which is achievable is certain materials [70]. To keep the bottom of the band structure fixed, we shift the FM bandstructure down by the value of J_{FM}, in both the FM leads. The chosen value for the Fermi level is $E_f = -2.1\ eV$, which lies deep inside the insulating gap and is close to the bottom of both the AFM and FM bands.

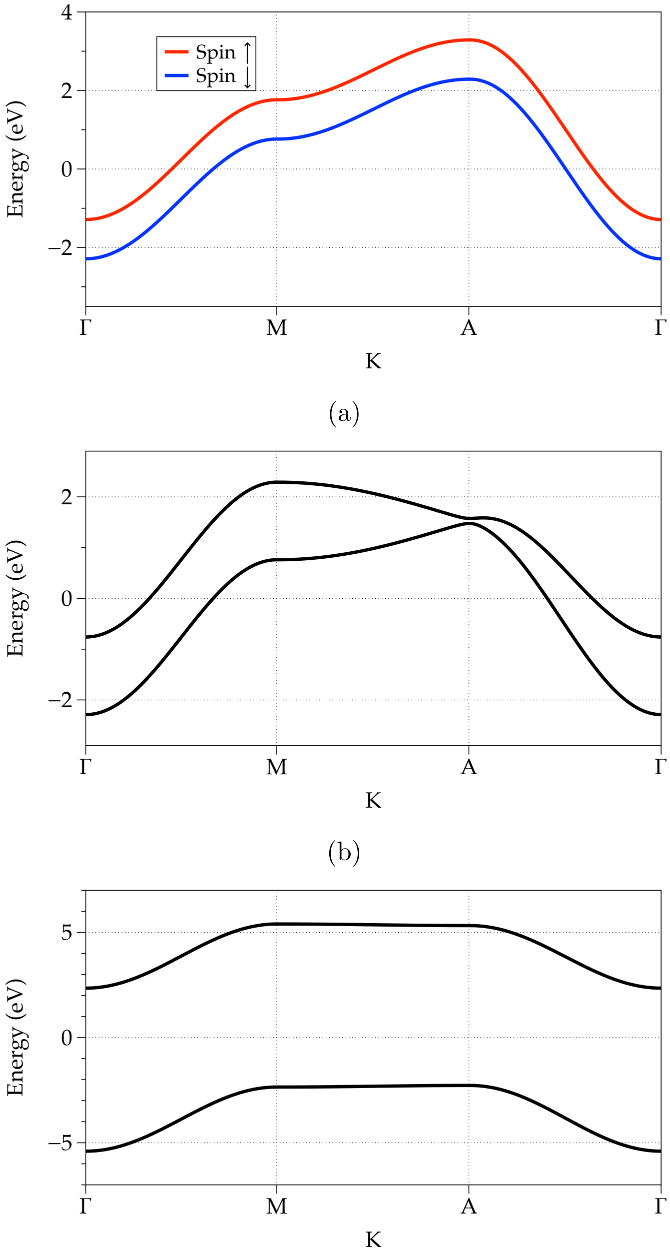

(a)

(b)

(c)

Figure 4.2: (a) Ferromagnetic band structure with $J_{SFM} = 0.5\ eV$ belongs to the soft ferromagnetic lead. The chosen Fermi level is $E_f = -2.1$ eV. Therefore the injected current is from a single spin-polarized band and near the Γ point. (b) AFM bandstructure with $J_{AFM} = 40$ meV. The two bands are spin-degenerate. (c) Insulator bandstructure with $m = 3.8$ eV.

4.2.2 Transport

To calculate the tunneling magnetoresistance, the nonequilibrium Green's function is employed. The retarded greens function of the system is:

$$G^R(E) = [E(I + i\eta)I - H - \Sigma_L - \Sigma_R]^{-1} \tag{4.5}$$

$\Sigma_{L,R}$ are the leads self energies and η is an infinitesimally small number. The transmission of the system is calculated from the retarded Green's function as below:

$$T(E) = \text{trace}[\Gamma_L G^R \Gamma_R G^A] \tag{4.6}$$

where $G^A = G^R$ and $\Gamma_{L,R} = -2\text{Im}[\Sigma_{L,R}]$ is the broadening of the left and right contacts. Finally, in the linear response regime, the conductance of the device is calculated as

$$G = -\frac{e^2}{h} \sum_{\sigma} \int \; dk_{x,y} \; T_\sigma(E_f) \; (\frac{\partial f}{\partial E})_{E=E_f}. \tag{4.7}$$

The conductance is calculated at zero temperature so that $-\partial f/\partial E = \delta(E - E_f)$.

4.3 Results and disscussion

4.3.1 TMR of magnetic Skyrmions

To better understand the effect of the hard magnet on the TMR, we temporarily eliminate the AFM layer from the device region (green) in Fig. 4.1 and replace it with another ferromagnet to investigate how the value of the exchange potential in the hard magnet changes the tunneling resistance. Fig. 4.3 shows the polarization of the HM as a function of J_{HM}, which is the exchange potential of the hard magnet. The polarization is calculated as $P = (D_{\uparrow} - D_{\downarrow})/(D_{\uparrow} + D_{\downarrow})$ for a bulk ferromagnet. D_{σ} is the electron density at the Fermi level. $D_{\downarrow}$ is constant since the down-spin band is fixed. On the other hand, by increasing J_{HM} from zero, the bottom of the up-spin band moves toward the Fermi level. The density of states of bulk materials is proportional to $\sqrt{E}$, therefore $D_{\uparrow}$ decreases with J_{HM}.

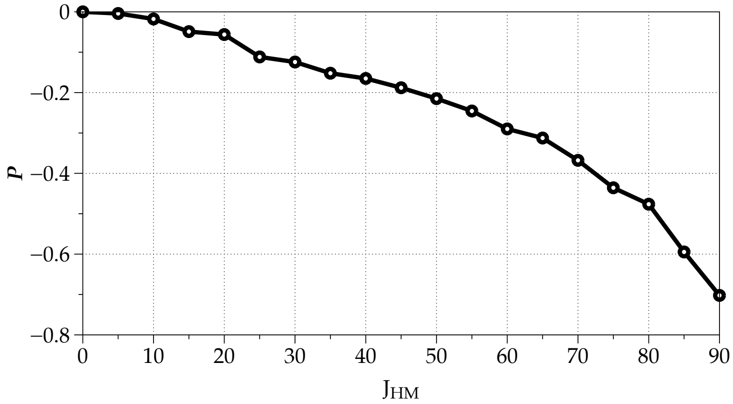

Figure 4.3: Polarization of the hard magnet vs. J_{HM}. Up-spin electrons density gradually decreases by increasing J_{HM} since the bottom of the up-spin band moves toward the Fermi level.

Now we put a magnetic Skyrmion in the device region to evaluate how it effects the transport and the TMR. The magnetization of a single Skyrmion is described by :

$$n(r) = [\sin\gamma(r)\cos\varphi(\phi), \sin\gamma(r)\sin\varphi(\phi), \cos\gamma(r)] \tag{4.8}$$

where $\varphi(\phi) = m\phi + \upsilon$ and $\phi = tan^{-1}(\frac{y}{x})$ and the term "υ" determines the helicity of Skyrmion. In this chapter, we only study Bloch-type Skyrmions (m = 1, $\upsilon = \pi/2$). Therefore

$\gamma(r=0)=0$, $\gamma(0<r<R)=\pi(1-\frac{r}{R})$, and $\gamma(r>R)=\pi$.

To implement a Skyrmion, we use a square cross-section made of 15×15 gridpoints, and to make it infinitely large, we apply the periodic boundary conditions. The diameter of the Skyrmion is also 13 gridpoints. Considering that the discretization length is about 5 Å, the Skyrmion diameter is about 6.5 nm. The thickenss of the device region is fixed to be 5 nm (10 layers) in all calculations, and the insulating barrier thickness is set to be 2 nm.

The TMR in the presence (MSKX) and absence (FM) of a magnetic Skyrmion in the device region is shown in Fig. 4.4a. Θ is the angle between the magnetic moment of the two magnetic leads . The ferromagnetic exchange potential in the device (J_{device}) and the hard magnet (J_{HM}) is set to be 85 meV. At $\Theta=0$, the FM device shows a lower resistance since it has the same magnetic moment as the two leads. By rotating the magnetic moment of the injected current, the FM device resistance increases with a significantly higher steep in comparison to the MSKX device. The maximum difference in the TMR occurs at $\Theta=\pi$, where the FM device resistance is 12.65 times higher than the MSKX device. To understand how the Skyrmion affects transport, we use a Stern-Gerlach apparatus analogy. In Fig. 4.4b, the two ferromagnetic leads are replaced with $\hat{z}$ polarizers. Since the FM device is a ferromagnet without a Skyrmion, it is also a $\hat{z}$ polarizer. Therefore it can not change the eigenstate of the incident electron from the left lead (SFM). When the two leads polarization is anti-aligned, the electron is blocked by the right lead (HM). However, by looking at a Skyrmion spatial spin configuration, we can replace a Skyrmion with a $\hat{x}$ polarizer. An incident electron with $S_z=\pm\frac{\hbar}{2}$ collapses two one of $S_x=\pm\frac{\hbar}{2}$ eigenstates with the same probability.

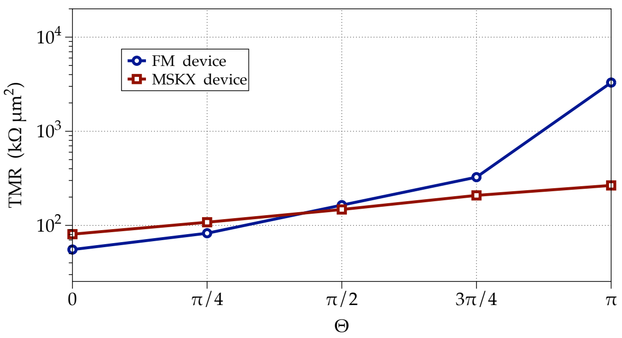

(a)

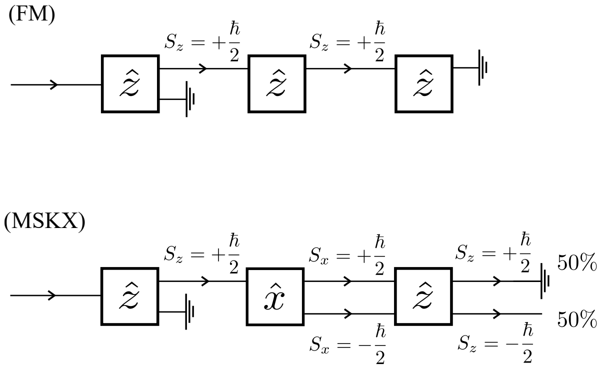

(b)

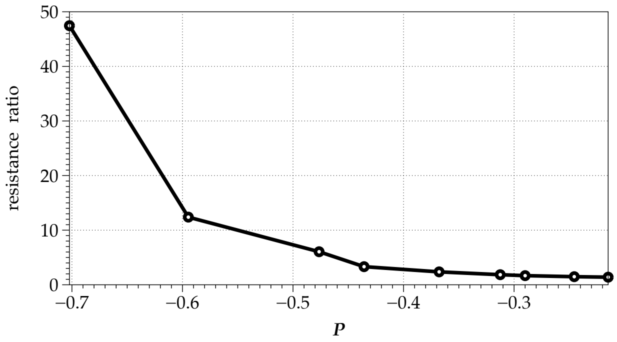

(c)

Figure 4.4: (a) Tunneling magnetoresistance as a function of Θ, in the presence (MSKX) and absence (FM) of a magnetic Skyrmion in the device region. Θ is the angle between the spin polarization of the two magnetic leads. The exchange potential of the hard FM (J_{HM}) is set to be 85 meV (P = -0.594). (b)The Stern-Gerlach apparatus analogy. The device region is the middle polarizer. The FM device is a $\hat{z}$ polarizer, which does not change the magnetic moment of injected current. The MSKX is analogous to a $\hat{x}$ polarizer, which changes the eigenstate of the injected current to $S_z = \frac{\hbar}{2}$. Electrons that leave the $\hat{x}$ polarizer can propagate in the right lead with the same probability. (c) The ratio of FM TMR to MSKX TMR at $\Theta = \pi$, plotted as a function of polarization ($J_{device} = J_{HM}$).

The electron with the new eigenstate also travels in the right magnet eigenstates ($S_z = \pm\frac{\hbar}{2}$) with the same transmission probability. Therefore it becomes insensitive to the Θ. The slight change in the MSKX TMR corresponds to the resistance of the pillar area, which is not covered by the Skyrmion and has the same polarization as the hard magnet.

We intend to block the injected current in the absence of Skyrmion and let the current flow to the hard magnet in the presence of Skyrmion. Then we can read-out Skyrmion whenever it passes under the magnetic probe in racetrack memories. Therefore the change that Skyrmion causes in the TMR is important. We define the resistance ratio as the ratio of TMR in the absence of Skyrmion to TMR in the presence of Skyrmion. The effect of the polarization on the resistance ratio (TMR_{FM}/TMR_{MSKX}) is plotted in Fig. 4.4c. We calculated the resistance for different values of J_{HM} ($J_{device} = J_{HM}$) and mapped it onto the polarization. The ratio is enhanced directly by increasing the polarization. This is because the injected current is most likely blocked by the hard magnet when the polarization is higher, but the MSKX is not sensitive to the polarization of the hard magnet.

4.3.2 TMR of AFM Skyrmions

In this section, we replace the ferromagnetic device with an AFM device, and we calculate the TMR to investigate the effect of AFM Skyrmion(ASKX) on the transport properties. An antiferromagnetic Skyrmion can be considered as a stack of two magnetic Skyrmions that are antiferromagnetically coupled.

The TMR, as a function of Θ is shown in Fig. 4.5a. The Néel vector of the AFM is along the transport direction ($S_z = \pm\frac{\hbar}{2}$), and $J_{device} = J_{HM} = 85$ meV. Similar to Fig. 4.4a, in the absence of Skyrmion, the TMR rises faster with Θ, and at $\Theta = \pi$, the resistance ratio is at its maximum. The big difference here is that the AFM device with a $\hat{z}$ Néel vector does not block the current as much as the FM device does. Therefore the resistance ratio is smaller, and the maximum ratio is 2.86 which occurs at $P = -0.7$.

To understand why the AFM Skyrmion works as a $\hat{x}$ polarizer and reduces the TMR, we replaced it with a $\hat{x}$ AFM and plotted the spin-precision of the injected current with respect to its initial phase as travels in the device region in Fig. 4.6. Since the AFM Skyrmion includes S_x and S_y components, a 1-D AFM chain with the Néel vector in the $\hat{x}$ direction captures the essential behavior as the presence of an AFM Skyrmion. Φ is the polar angle of the left-injected spinor calculated at each site from $\langle\psi_i|\sigma_z|\psi_i\rangle/\sqrt{\langle\psi_i|\psi_i\rangle}$, where ψ_i is the left-injected wavefunction at site i. The AFM device Néel vector is along the $\hat{x}$ direction, and Φ is calculated at the Fermi level with $k_x = k_y = 0$. In Fig. 4.6a, the angle of the injected current is zero at the left lead. When the up-spin electron ($\Phi = 0$) travels through the device, Φ acquires a non-zero value at each gridpoint. When it reaches the right lead, it has some $-S_z$ component. If the leads spin-polarization is anti-aligned, the transmission occurs due to this deviation from the initial angle. By increasing the value of J_{AFM} we increased the deviation from the initial angle, which means a larger -S_z component and more transmission. For $J_{AFM} = 50$ meV Φ is 17.4° and it increases up to $\Phi = 24.1°$ at $J_{AFM} = 120$ meV. The existence of a tunneling barrier, as shown in Fig. 4.6b, can slightly increase Φ and decrease the resistance ratio. For $J_{AFM} = 120m\ eV$ in the presence of the tunneling barrier, the Φ becomes 28.6°.

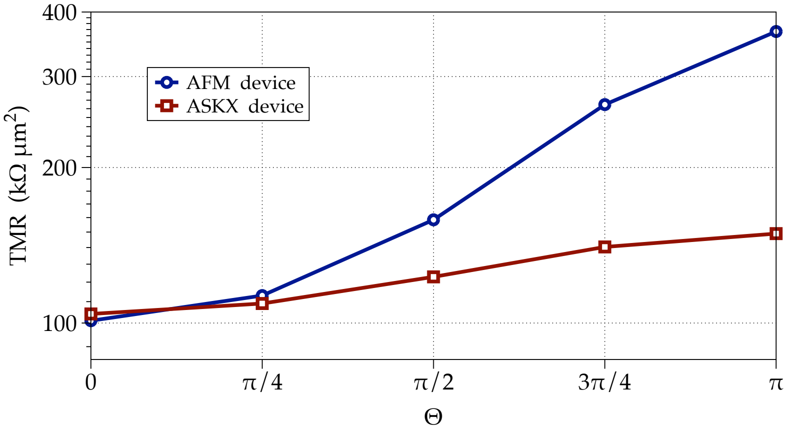

(a)

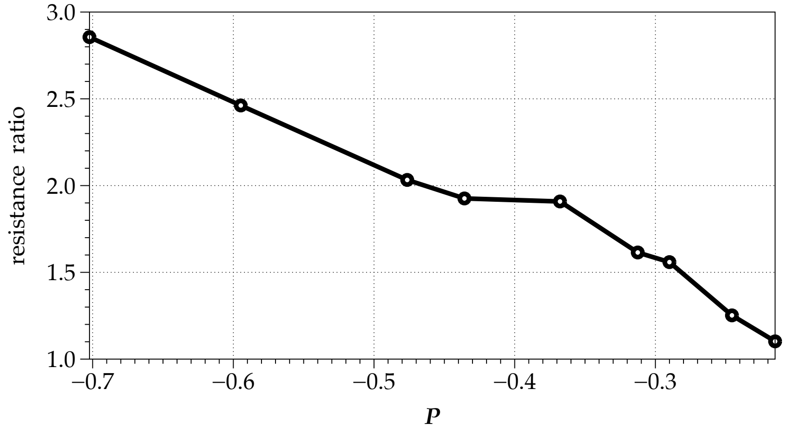

(b)

Figure 4.5: (a) TMR vs. Θ for an antiferromagnetic (AFM) device and AFM Skyrmion (ASKX). $J_{AFM} = J_{HM} = 85$ meV and the insulating barrier thickness is 2 nm. (b) The resistance ratio (TMR_{AFM}/TMR_{ASKX}), at $\Theta = \pi$. $(J_{device} = J_{HM})$

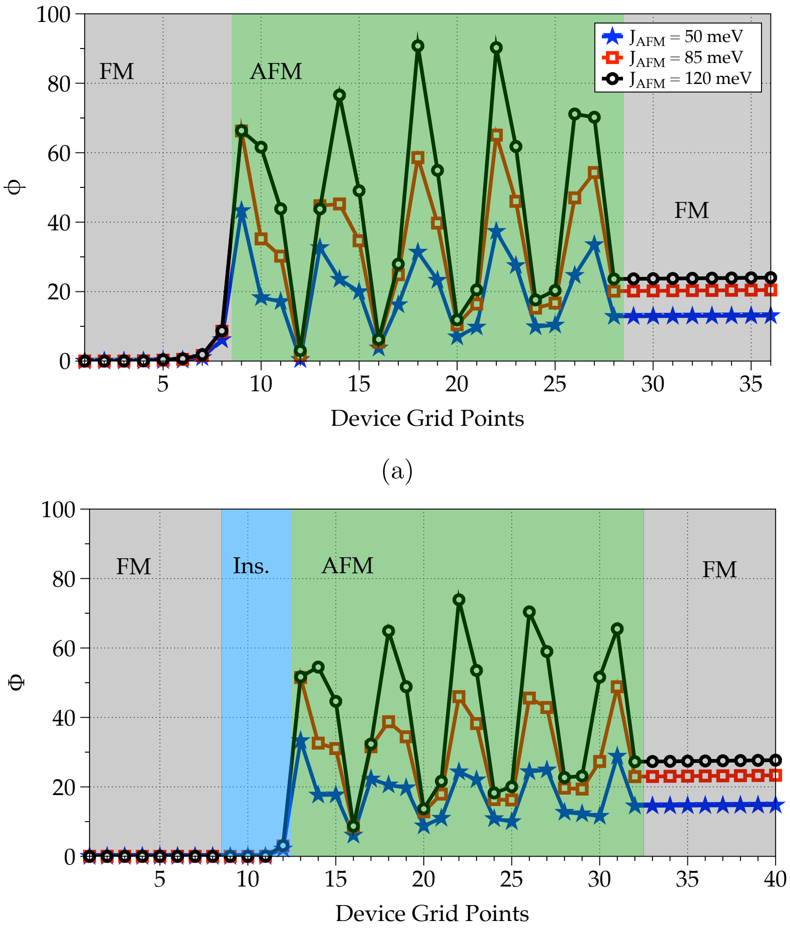

(a)

(b)

Figure 4.6: The polar angle Φ of the injected upspin as it travels in the device region. (a) Without an insulating barrier. (b) The thickness of the barrier is 2nm. When the current leaves the left lead, it has no -S_z component. However, when it reaches to the right lead, it gains some -S_z component and deviates from its initial angle. This deviation depends on the strength of the AFM exchange potential. (Φ is the angle between the injected current magnetic moment and the transport direction)

4.4 Conclusion

In summary, magneto tunneling resistance can be employed to detect Skyrmion spin textures in layered synthetic antiferromagnetic materials. We calculated the resistance of a ferromagnet/insulator/antiferromagnet/ferromagnet heterostructure in the presence and absence of a Skyrmion. The top ferromagnetic lead is used as a magnetic probe to inject a spin-polarized current into the device. The hard bottom magnet works as a $\hat{z}$ polarizer that filters out the injected current. We showed that, in the presence of a magnetic or an antiferromagnetic Skyrmion, the tunneling magnetoresistance is much less sensitive to whetever the magnetic leads are aligned or anti-aligned. The change in the resistance caused by the presence of Skyrmion is a tool for the detection and read-out process of Skyrmions in race track memories. This resistance ratio can reach up to 100 in the FM Skyrmion device and up to 8 in the AFM Skyrmion device. This ratio can be engineered by the magnitude of antiferromagnetic exchange potential, the polarization of the magnetic leads, and the existence of a tunneling barrier.

Bibliography

[1] Nima Djavid, Gen Yin, Yafis Barlas, and Roger K. Lake. Gate controlled Majorana zero modes of a two-dimensional topological superconductor. *Applied Physics Letters*, 113(1):012601, 2018.

[2] Sankar Das Sarma, Michael Freedman, and Chetan Nayak. Majorana zero modes and topological quantum computation. *npj Quantum Information*, 1(1):15001, dec 2015.

[3] Sergey Bravyi. Universal quantum computation with the ν=5/2 fractional quantum Hall state. *Physical Review A - Atomic, Molecular, and Optical Physics*, 73(4):042313, apr 2006.

[4] Sergey Bravyi and Alexei Kitaev. Universal quantum computation with ideal Clifford gates and noisy ancillas. *Physical Review A - Atomic, Molecular, and Optical Physics*, 71(2):022316, feb 2005.

[5] Albert Fert, Vincent Cros, and João Sampaio. Skyrmions on the track. *Nature Nanotechnology*, 8(3):152–156, mar 2013.

[6] A. Yu Kitaev. Fault-tolerant quantum computation by anyons. *Annals of Physics*, 303(1):2–30, jan 2003.

[7] Ettore Majorana and Luciano Maiani. A symmetric theory of electrons and positrons. In *Ettore Majorana Scientific Papers*, pages 201–233. Springer, Berlin, Heidelberg, 2006. DOI: 10.1007/978-3-540-48095-2_10.

[8] Liang Fu and C L Kane. Superconducting {Proximity} {Effect} and {Majorana} {Fermions} at the {Surface} of a {Topological} {Insulator}. *Phys. Rev. Lett.*, 100(9):96407, 2008.

[9] A Yu Kitaev. Unpaired Majorana fermions in quantum wires. *Physics-Uspekhi*, 44(10S):131–136, oct 2001.

[10] N. Read and Dmitry Green. Paired states of fermions in two dimensions with breaking of parity and time-reversal symmetries and the fractional quantum Hall effect. *Physical Review B - Condensed Matter and Materials Physics*, 61(15):10267–10297, apr 2000.

[11] N. B. Kopnin and M. M. Salomaa. Mutual friction in superfluid He3: Effects of bound states in the vortex core. *Physical Review B*, 44(17):9667–9677, nov 1991.

[12] Jing Wang, Quan Zhou, Biao Lian, and Shou Cheng Zhang. Chiral topological superconductor and half-integer conductance plateau from quantum anomalous Hall plateau transition. *Physical Review B - Condensed Matter and Materials Physics*, 92(6):064520, aug 2015.

[13] Quan Zhou, Shou-Cheng Zhang, Yabin Fan, Eun Sang Choi, Jing Xia, Kang L. Wang, Qing Lin He, Edward C. Burks, Gen Yin, Kai Liu, Qiming Shao, Koichi Murata, Lei Pan, Xufeng Kou, Biao Lian, Zhijie Chen, Xiaoyu Che, Tianxiao Nie, Alexander L. Stern, and Jing Wang. Chiral Majorana fermion modes in a quantum anomalous Hall insulator–superconductor structure. *Science*, 357(6348):294–299, 2017.

[14] Eryin Wang, Hao Ding, Alexei V. Fedorov, Wei Yao, Zhi Li, Yan Feng Lv, Kun Zhao, Li Guo Zhang, Zhijun Xu, John Schneeloch, Ruidan Zhong, Shuai Hua Ji, Lili Wang, Ke He, Xucun Ma, Genda Gu, Hong Yao, Qi Kun Xue, Xi Chen, and Shuyun Zhou. Fully gapped topological surface states in Bi 2 Se 3 films induced by a d-wave high-temperature superconductor. *Nature Physics*, 9(10):621–625, 2013.

[15] T. Jungwirth, X. Marti, P. Wadley, and J. Wunderlich. Antiferromagnetic spintronics. *Nature Nanotechnology*, 11(3):231–241, mar 2016.

[16] Joseph Barker and Oleg A. Tretiakov. Static and Dynamical Properties of Antiferromagnetic Skyrmions in the Presence of Applied Current and Temperature. *Physical Review Letters*, 116(14):147203, apr 2016.

[17] Xichao Zhang, Yan Zhou, and Motohiko Ezawa. Magnetic bilayer-skyrmions without skyrmion Hall effect. *Nature Communications*, 7, 2016.

[18] William Legrand, Davide Maccariello, Fernando Ajejas, Sophie Collin, Aymeric Vecchiola, Karim Bouzehouane, Nicolas Reyren, Vincent Cros, and Albert Fert. Room-temperature stabilization of antiferromagnetic skyrmions in synthetic antiferromagnets. *Nature Materials*, pages 1–23, sep 2019.

[19] A. Yu Kitaev. Unpaired Majorana fermions in quantum wires. *Physics-Uspekhi*, 44(10S):131, 2001.

[20] Liang Fu and C. L. Kane. Superconducting Proximity Effect and Majorana Fermions at the Surface of a Topological Insulator. *Physical Review Letters*, 100(9):096407, March 2008.

[21] M. Wimmer, A. R. Akhmerov, M. V. Medvedyeva, J. Tworzydło, and C. W. J. Beenakker. Majorana bound states without vortices in topological superconductors with electrostatic defects. *Phys. Rev. Lett.*, 105(4):046803, 2010.

[22] S. R. Elliott and M. Franz. Colloquium: Majorana fermions in nuclear, particle, and solid-state physics. *Rev. Mod. Phys.*, 87(1):137–163, 2015.

[23] V. Mourik, K. Zuo, S. M. Frolov, S. R. Plissard, E. P. a. M. Bakkers, and L. P. Kouwenhoven. Signatures of Majorana Fermions in Hybrid Superconductor-Semiconductor Nanowire Devices. *Science*, 336(6084):1003–1007, May 2012.

[24] M. T. Deng, S. Vaitiekėnas, E. B. Hansen, J. Danon, M. Leijnse, K. Flensberg, J. Nygård, P. Krogstrup, and C. M. Marcus. Majorana bound state in a coupled quantum-dot hybrid-nanowire system. *Science*, 354(6319):1557–1562, December 2016.

[25] Jason Alicea, Yuval Oreg, Gil Refael, Felix von Oppen, and Matthew P. A. Fisher. Non-Abelian statistics and topological quantum information processing in 1d wire networks. *Nature Physics*, 7(5):412, May 2011.

[26] A. Yu. Kitaev. Fault-tolerant quantum computation by anyons. *Annals of Physics*, 303(1):2–30, January 2003.

[27] Jason Alicea. New directions in the pursuit of Majorana fermions in solid state systems. *Reports on Progress in Physics*, 75(7):076501, 2012.

[28] David Aasen, Michael Hell, Ryan V. Mishmash, Andrew Higginbotham, Jeroen Danon, Martin Leijnse, Thomas S. Jespersen, Joshua A. Folk, Charles M. Marcus, Karsten Flensberg, and Jason Alicea. Milestones Toward Majorana-Based Quantum Computing. *Physical Review X*, 6(3):031016, August 2016.

[29] Sébastien R. Plissard, Ilse van Weperen, Diana Car, Marcel A. Verheijen, George W. G. Immink, Jakob Kammhuber, Ludo J. Cornelissen, Daniel B. Szombati, Attila Geresdi, Sergey M. Frolov, Leo P. Kouwenhoven, and Erik P. A. M. Bakkers. Formation and electronic properties of InSb nanocrosses. *Nature Nanotechnology*, 8(11):859, November 2013.

[30] M. Hell, M. Leijnse, and K. Flensberg. Two-dimensional platform for networks of majorana bound states. *Phys. Rev. Lett.*, 118:107701, 2017.

[31] Qing Lin He, Lei Pan, Alexander L. Stern, Edward C. Burks, Xiaoyu Che, Gen Yin, Jing Wang, Biao Lian, Quan Zhou, Eun Sang Choi, Koichi Murata, Xufeng Kou, Zhijie Chen, Tianxiao Nie, Qiming Shao, Yabin Fan, Shou-Cheng Zhang, Kai Liu, Jing Xia, and Kang L. Wang. Chiral Majorana fermion modes in a quantum anomalous Hall insulator–superconductor structure. *Science*, 357(6348):294–299, July 2017.

[32] Biao Lian, Jing Wang, and Shou-Cheng Zhang. Edge-state-induced Andreev oscillation in quantum anomalous Hall insulator-superconductor junctions. *Physical Review B*, 93(16):161401, April 2016.

[33] Jing Wang, Quan Zhou, Biao Lian, and Shou-Cheng Zhang. Chiral topological superconductor and half-integer conductance plateau from quantum anomalous Hall plateau transition. *Physical Review B*, 92(6):064520, August 2015.

[34] Chui-Zhen Chen, James Jun He, Dong-Hui Xu, and K. T. Law. Effects of domain walls in quantum anomalous Hall insulator/superconductor heterostructures. *Physical Review B*, 96(4):041118, July 2017.

[35] Hao-Hua Sun, Kai-Wen Zhang, Lun-Hui Hu, Chuang Li, Guan-Yong Wang, Hai-Yang Ma, Zhu-An Xu, Chun-Lei Gao, Dan-Dan Guan, Yao-Yi Li, Canhua Liu, Dong Qian, Yi Zhou, Liang Fu, Shao-Chun Li, Fu-Chun Zhang, and Jin-Feng Jia. Majorana Zero Mode Detected with Spin Selective Andreev Reflection in the Vortex of a Topological Superconductor. *Physical Review Letters*, 116(25):257003, June 2016.

[36] Y. Kim, T. M. Philip, M. J. Park, and M. J. Gilbert. Topological superconductivity in an ultrathin, magnetically-doped topological insulator proximity coupled to a conventional superconductor. *Phys. Rev. B*, 94:235434, 2016.

[37] Yongxin Zeng, Chao Lei, Gaurav Chaudhary, and Allan H. MacDonald. Quantum anomalous Hall Majorana platform. *Physical Review B*, 97(8):081102, February 2018.

[38] Chui-Zhen Chen, Ying-Ming Xie, Jie Liu, Patrick A. Lee, and K. T. Law. Quasi-one-dimensional Quantum Anomalous Hall Systems as New Platforms for Scalable Topological Quantum Computation. *arXiv:1709.10474 [cond-mat]*, September 2017.

[39] Suk Bum Chung, Xiao-Liang Qi, Joseph Maciejko, and Shou-Cheng Zhang. Conductance and noise signatures of Majorana backscattering. *Physical Review B*, 83(10):100512, March 2011.

[40] Michael Schackert Peter. *Tunneling Spectroscopy on Electron-Boson Interactions in Superconductors*. KIT Scientific Publishing, March 2015.

[41] Jian-Min Zhang, Ruqian Lian, Yanmin Yang, Guigui Xu, Kehua Zhong, and Zhigao Huang. Engineering Topological Surface State of Cr-doped Bi_2Se_3 under external electric field. *Scientific Reports*, 7:43626, March 2017.

[42] Yi Zhang, Ke He, Cui-Zu Chang, Can-Li Song, Li-Li Wang, Xi Chen, Jin-Feng Jia, Zhong Fang, Xi Dai, Wen-Yu Shan, Shun-Qing Shen, Qian Niu, Xiao-Liang Qi, Shou-Cheng Zhang, Xu-Cun Ma, and Qi-Kun Xue. Crossover of the three-dimensional topological insulator Bi_2Se_3 to the two-dimensional limit. *Nature Physics*, 6(8):584, August 2010.

[43] Chao-Xing Liu, Xiao-Liang Qi, HaiJun Zhang, Xi Dai, Zhong Fang, and Shou-Cheng Zhang. Model Hamiltonian for topological insulators. *Physical Review B*, 82(4):045122, July 2010.

[44] D. Gershoni, C. H. Henry, and G. A. Baraff. Calculating the optical properties of multidimensional heterostructures: application to the modeling of quaternary quantum well lasers. *IEEE J. Quantum Electron.*, 29(9):2433, 1993.

[45] R. Lake, G. Klimeck, R. C. Bowen, and D. Jovanovic. Single and multi-band modeling of quantum electron transport through layered semiconductor devices. *J. Appl. Phys.*, 81(12):7845–7869, 1997.

[46] M. P. Lopez Sancho, J. M. Lopez Sancho, and J. Rubio. Highly convergent schemes for the calculation of bulk and surface green functions. *J. Phys. F*, 15:851–858, 1985.

[47] M. Galperin, S. Toledo, and A. Nitzan. Numerical computation of tunneling fluxes. *J. Chem. Phys.*, 117:10817–10826, 2002.

[48] Mahdi Mashkoori and Annica Black-Schaffer. Majorana bound states in magnetic impurity chains: effects of \$d\$-wave pairing. Technical report, 2018.

[49] Hiromi Ebisu, Keiji Yada, Hideaki Kasai, and Yukio Tanaka. Majorana edge states and topological properties in 1D/2D Rashba semiconductor proximity coupled to iron-based superconductor. *Superconductor Science and Technology*, 28(1):014001, 2015.

[50] Zhongbo Yan, Fei Song, and Zhong Wang. Majorana Corner Modes in a High-Temperature Platform. *Physical Review Letters*, 121(9), 2018.

[51] Dongfei Wang, Lingyuan Kong, Peng Fan, Hui Chen, Shiyu Zhu, Wenyao Liu, Lu Cao, Yujie Sun, Shixuan Du, John Schneeloch, Ruidan Zhong, Genda Gu, Liang Fu, Hong Ding, and Hong Jun Gao. Evidence for Majorana bound states in an iron-based superconductor. *Science*, 362(6412):333–335, oct 2018.

[52] Keita Hamamoto, Motohiko Ezawa, and Naoto Nagaosa. Quantized topological Hall effect in skyrmion crystal. *Physical Review B*, 92(11):115417, sep 2015.

[53] Akito Daido and Youichi Yanase. Majorana flat bands, chiral Majorana edge states, and unidirectional Majorana edge states in noncentrosymmetric superconductors. *Physical Review B*, 95(13):134507, apr 2017.

[54] Masatoshi Sato and Satoshi Fujimoto. Existence of Majorana fermions and topological order in nodal superconductors with spin-orbit interactions in external magnetic fields. *Physical Review Letters*, 105(21), 2010.

[55] Tôru Moriya. New Mechanism of Anisotropic Superexchange Interaction. *Physical Review Letters*, 4(5):228–230, 1960.

[56] I. Dzyaloshinsky. A thermodynamic theory of ”weak” ferromagnetism of antiferromagnetics. *Journal of Physics and Chemistry of Solids*, 4(4):241–255, jan 1958.

[57] S. Seki, X. Z. Yu, S. Ishiwata, and Y. Tokura. Observation of skyrmions in a multiferroic material. *Science*, 336(6078):198–201, apr 2012.

[58] B Lebech, J Bernhard, and T Freltoft. Magnetic structures of cubic FeGe studied by small-angle neutron scattering. *Journal of Physics: Condensed Matter*, 1(35):6105–6122, sep 1989.

[59] H. Wilhelm, M. Baenitz, M. Schmidt, U. K. Rößler, A. A. Leonov, and A. N. Bogdanov. Precursor phenomena at the magnetic ordering of the cubic helimagnet FeGe. *Physical Review Letters*, 107(12):1–5, 2011.

[60] Chendong Jin, Chengkun Song, Jianbo Wang, and Qingfang Liu. Dynamics of antiferromagnetic skyrmion driven by the spin Hall effect. *Applied Physics Letters*, 109(18):182404, oct 2016.

[61] William Legrand, Davide Maccariello, Fernando Ajejas, Sophie Collin, Aymeric Vecchiola, Karim Bouzehouane, Nicolas Reyren, Vincent Cros, and Albert Fert. Room-temperature stabilization of antiferromagnetic skyrmions in synthetic antiferromagnets. *Nature Materials*, pages 1–9, sep 2019.

[62] Christian Hanneken, Fabian Otte, André Kubetzka, Bertrand Dupé, Niklas Romming, Kirsten von Bergmann, Roland Wiesendanger, and Stefan Heinze. Electrical detection of magnetic skyrmions by tunnelling non-collinear magnetoresistance. *Nature Nanotechnology*, 10(12):1039–1042, dec 2015.

[63] Davide Maccariello, William Legrand, Nicolas Reyren, Karin Garcia, Karim Bouzehouane, Sophie Collin, Vincent Cros, and Albert Fert. Electrical detection of single magnetic skyrmions in metallic multilayers at room temperature. *Nature Nanotechnology*, 13(3):233–237, mar 2018.

[64] Shasha Wang, Jin Tang, Weiwei Wang, Lingyao Kong, Mingliang Tian, and Haifeng Du. Electrical Detection of Magnetic Skyrmions. *Journal of Low Temperature Physics*, pages 1–16, jun 2019.

[65] Keita Hamamoto, Motohiko Ezawa, and Naoto Nagaosa. Purely electrical detection of a skyrmion in constricted geometry. *Applied Physics Letters*, 108(11):112401, mar 2016.

[66] Riccardo Tomasello, Marco Ricci, Pietro Burrascano, Vito Puliafito, Mario Carpentieri, and Giovanni Finocchio. Electrical detection of single magnetic skyrmion at room temperature. *AIP Advances*, 7(5):056022, may 2017.

[67] André Kubetzka, Christian Hanneken, Roland Wiesendanger, and Kirsten Von Bergmann. Impact of the skyrmion spin texture on magnetoresistance. *Physical Review B*, 95(10):104433, mar 2017.

[68] Roland Wiesendanger. Spin mapping at the nanoscale and atomic scale. *Reviews of Modern Physics*, 81(4):1495–1550, nov 2009.

[69] Patrick M. Buhl, Frank Freimuth, Stefan Blügel, and Yuriy Mokrousov. Topological spin Hall effect in antiferromagnetic skyrmions. *Physica Status Solidi - Rapid Research Letters*, 11(4):1700007, apr 2017.

[70] M. Bowen, A. Barthélémy, M. Bibes, E. Jacquet, J. P. Contour, A. Fert, D. Wortmann, and S. Blügel. Half-metallicity proven using fully spin-polarized tunnelling. *Journal of Physics Condensed Matter*, 17(41):L407–L409, oct 2005.

[71] Roland Wiesendanger. Nanoscale magnetic skyrmions in metallic films and multilayers: A new twist for spintronics. *Nature Reviews Materials*, 1(7):16044, jul 2016.

[72] R. M. Lutchyn, E. P. A. M. Bakkers, L. P. Kouwenhoven, P. Krogstrup, C. M. Marcus, and Y. Oreg. Realizing majorana zero modes in superconductor-semiconductor heterostructures. *arXiv:1707.04899v2*, 2018.

[73] M P Lopez Sancho, J M Lopez Sancho, and J Rubio. Quick iterative scheme for the calculation of transfer matrices: application to mo (100). *Journal of Physics F: Metal Physics*, 14(5):1205, 1984.

[74] Yongxin Zeng, Chao Lei, Gaurav Chaudhary, and Allan H. MacDonald. The Quantum Anomalous Hall Majorana Platform. *arXiv:1710.06823 [cond-mat]*, October 2017. arXiv: 1710.06823.

[75] Haijun Zhang, Chao-Xing Liu, Xiao-Liang Qi, Xi Dai, Zhong Fang, and Shou-Cheng Zhang. Topological insulators in Bi_2Se_3, Bi_2Te_3 and Sb_2Te_3 with a single Dirac cone on the surface. *Nature Physics*, 5(6):438, June 2009.

[76] Roger Lake and Supriyo Datta. Nonequilibrium Green's-function method applied to double-barrier resonant-tunneling diodes. *Physical Review B*, 45(12):6670–6685, March 1992.

[77] Eryin Wang, Hao Ding, Alexei V. Fedorov, Wei Yao, Zhi Li, Yan-Feng Lv, Kun Zhao, Li-Guo Zhang, Zhijun Xu, John Schneeloch, Ruidan Zhong, Shuai-Hua Ji, Lili Wang, Ke He, Xucun Ma, Genda Gu, Hong Yao, Qi-Kun Xue, Xi Chen, and Shuyun Zhou. Fully gapped topological surface states in Bi_2Se_3 films induced by a d-wave high-temperature superconductor. *Nature Physics*, 9(10):621, October 2013.

[78] D. J. J. Marchand and M. Franz. Lattice model for the surface states of a topological insulator with applications to magnetic and exciton instabilities. *Physical Review B*, 86(15):155146, October 2012.

[79] Xiao-Liang Qi, Taylor L. Hughes, and Shou-Cheng Zhang. Chiral topological superconductor from the quantum Hall state. *Physical Review B*, 82(18):184516, November 2010.

[80] M. Ezawa. Topological phase transition and electrically tunable diamagnetism in silicene. *The European Physical Journal B*, 85(11):363, November 2012.

[81] Sayed Ali Akbar Ghorashi, Xiang Hu, Taylor L. Hughes, and Enrico Rossi. Second-order Dirac superconductors and magnetic field induced Majorana hinge modes. *Physical Review B*, 100(2), jan 2019.

[82] Biao Lian, Xiao Qi Sun, Abolhassan Vaezi, Xiao Liang Qib, and Shou Cheng Zhang. Topological quantum computation based on chiral Majorana fermions. *Proceedings of the National Academy of Sciences of the United States of America*, 115(43):10938–10942, 2018.

[83] J. A. Sauls. Andreev bound states and their signatures. *Philosophical Transactions of the Royal Society A: Mathematical, Physical and Engineering Sciences*, 376(2125), 2018.

[84] Soniya Balram and M. Wilscy. User traffic profile for traffic reduction and effective bot C&C detection. *International Journal of Network Security*, 16(1):46–52, 2014.

[85] Fan Zhang and Wei Pan. A missing step is a key step. *Nature Materials*, 17(10):851–852, 2018.

[86] Chui-Zhen Chen, James Jun He, Dong-Hui Xu, and K. T. Law. Emergent Josephson current of $N=1$ chiral topological superconductor in quantum anomalous Hall insulator/superconductor heterostructures. *Physical Review B*, 98:165439, 2018.

[87] Hai Bin Wu, Ying Tao Zhang, and Jian Jun Liu. The tunneling magnetoresistance in 2D topological superconductor hybrid structure. *Journal of Applied Physics*, 124(8):84301, 2018.

[88] Yang Peng and Yong Xu. Proximity-induced Majorana hinge modes in antiferromagnetic topological insulators. Technical report, 2018.

[89] R. M. Lutchyn, E. P.A.M. Bakkers, L. P. Kouwenhoven, P. Krogstrup, C. M. Marcus, and Y. Oreg. Majorana zero modes in superconductor-semiconductor heterostructures. *Nature Reviews Materials*, 3(5):52–68, 2018.

[90] Mehdi Biderang, Heshmatollah Yavari, Mohammad Hossein Zare, Peter Thalmeier, and Alireza Akbari. Edge currents as a probe of the strongly spin-polarized topological noncentrosymmetric superconductors. *Physical Review B*, 98(1):14524, 2018.

[91] Mahdi Mashkoori, Kristofer Björnson, and Annica M. Black-Schaffer. Impurity bound states in fully gapped d-wave superconductors with subdominant order parameters. *Scientific Reports*, 7, 2017.

[92] Fan Zhang, C. L. Kane, and E. J. Mele. Time-reversal-invariant topological superconductivity and Majorana kramers pairs. *Physical Review Letters*, 111(5), 2013.

[93] P. J. Hirschfeld. Erratum: Corrigendum to “Using gap symmetry and structure to reveal the pairing mechanism in Fe-based superconductors” (Comptes Rendus Physique (2016) 17(1-2) (197–231)(S1631070515001693)(10.1016/j.crhy.2015.10.002)). *Comptes Rendus Physique*, 17(7):803, 2016.

[94] He Zhao, Bryan Rachmilowitz, Zheng Ren, Ruobin Han, J. Schneeloch, Ruidan Zhong, Genda Gu, Ziqiang Wang, and Ilija Zeljkovic. Superconducting proximity effect in a topological insulator using Fe(Te, Se). *Physical Review B*, 97(22):224504, 2018.

[95] S. Varona, L. Ortiz, O. Viyuela, and M. A. Martin-Delgado. Topological phases in nodeless tetragonal superconductors. *Journal of Physics Condensed Matter*, 30(39), 2018.

[96] K. Shibata, X. Z. Yu, T. Hara, D. Morikawa, N. Kanazawa, K. Kimoto, S. Ishiwata, Y. Matsui, and Y. Tokura. Towards control of the size and helicity of skyrmions in helimagnetic alloys by spin-orbit coupling. *Nature Nanotechnology*, 8(10):723–728, oct 2013.

Appendix A

Sparse NEGF solver tutorial

This section is a tutorial for using the c++ based simulator designed for electronic transport calculations of any 3D heterostructure. Features of this simulator are : Non-equilibrium Greens function is employed for the transport calculations. Recursive Greens function is implemented to find the Greens function from the open boundary Hamiltonian. Sparse matrix algebra is used to enable us to simulate very large structures. The decimation algorithm (Sancho) is implemented in the code to accelerate the surface Greens function calculations.

A.1 tutorial

A.1.1 Compiling the code

The code is written in c++, and we use a make file inside the code folder to compile our simulator. The required library for compilation is the "Eigen" library. The code is written in c++, and we use a make file inside the code folder to compile our simulator. The required library for compilation is the "Eigen" library. The location of the "Eigen" library is set in the make file as below :

```
src      =    $(wildcard     Code/*.cpp)
dep      =    $(wildcard     Code/*.hpp)
obj      =    $(src:.c=.o)
CC       =    g++     -std=c++0x
Flags    =    -g      -fopenmp      -O3     -march=native    -I
Include  =    "Set␣the␣location␣here␣!"    $(dep)
TARGET   =    OUTPUT

myprog:  $(obj)
         $(CC)    -o     $(TARGET)     $(Flags)$(Include)     $(src)

run:     myprog
         clear
```

```
        ./$(TARGET)


clean:
        clear
        rm    -rf    $(TARGET)*
        rm    -rf    *.log
        rm    -rf    *.dat


reset:
        rm    -rf    *.log
        rm    -rf    *.dat
```

After setting the location of the ”Eigen” library, we can compile code by using the ”make” command. To run or remove the executable file, the ”make run” and ”make clean” commands are used, respectively.

A.1.2 Input files

We use three different input files to set the geometry and spatial dependent variables for the code.

The first input file is the geometry file, which it can find the main folder as "Inputfile.txt". In this file, we define the geometry and some desirable variables that have a spatial dependency and take different values at different parts of the device. Below is an example of an "Inputfile.txt" file.

```
x y z Sx Sy Sz PG mu Eg isSC
0 0 0 0 0 1 0.500000 0.000000 0.000000 1
1 0 0 0 0 0 0.000000 0.000000 4.000000 0
2 0 0 0 0 1 0.500000 0.000000 0.000000 1
3 0 0 0 0 1 0.500000 0.000000 0.000000 1
0 1 0 0 0 1 0.500000 0.000000 0.000000 1
1 1 0 0 0 0 0.000000 0.000000 4.000000 0
2 1 0 0 0 1 0.500000 0.000000 0.000000 1
3 1 0 0 0 1 0.500000 0.000000 0.000000 1
```

As can be seen, each row is a gid point that contains some information such as spin polarization, Fermi level (μ), and superconductivity flag ($isSC$). We can add as many as columns we need to get more information inside the code. If any new column is added to the input file, we should make a small change in a file called "ElectronSystem.cpp".

```
// **************************************************** //
// ********  Read In Geometry definition  ************ //
// ************************************************** //
void ElectronSystem::ReadInGeometry(const char* InputFileName)
{
    int x, y, z, Sx, Sy, Sz, isAFM, isSC;
    int countSite = 0;
    int countTotalSize = 0;
    double E0, JH, PG_S, mu;

    Vector3d newSpin(0, 0, 0), newLocation(0, 0, 0);

    ifstream input(InputFileName);
    string line;
    getline(input, line);
    do {
        getline(input, line);
        if (line.empty() || input.eof())
            break;
        istringstream iss(line);
iss >> x >> y >> z >> Sx >> Sy >> Sz >> PG >> mu >> Eg >> isSC;
```

In the last line of the above function, each variable corresponds to a column in the input file. Therefore adding any column to the input file requires a new variable in the mentioned line of the code.

The other two input files are called "OpenBoundaries.txt" and "BoundariesShift.txt". Each row of the first file contains the grid points that are located at the open boundaries, and the corresponding row in the second file is the vector that expands the boundary in that direction.

An example of an "OpenBoundaries.txt" file :

$0 \;\; 1 \;\; 2 \;\; 3$

$4 \;\; 5 \;\; 6 \;\; 7$

An example of a "BoundariesShift.txt" file :

$-1 \;\; 0 \;\; 0$

$+ \;\; 0 \;\; 0$

A.1.3 Setting up the Hamiltonian

To set up the Hamiltonian in the code, it is required to discretize the analytical model and find the on-site block and coupling matrices. The on-site block is defined in the ”ElectronSite.cpp” file. The coupling blocks are defined in the ”ElectronSystem.cpp” file and inside the ”Couplingmtrices” function. Below in an example of an on-site block Hamiltonian of a superconductor.

```
this->OnSiteBlock.setZero(4, 4);


Matrix2cd PairingBlock;
PairingBlock << 0  , PG,
               -PG,  0;


this->OnSiteBlock(0, 0) = +mu;
this->OnSiteBlock(1, 1) = +mu;
this->OnSiteBlock(2, 2) = - mu;
this->OnSiteBlock(3, 3) = - mu;


this->OnSiteBlock.block(0, 2, 2, 2) = PairingBlock;
this->OnSiteBlock.block(2, 0, 2, 2) = PairingBlock.adjoint();
```

A.1.4 Sparse matrix library

The required functions for making and filling a sparse matrix is implemented in the "SparseMath.hpp" header file. To create a sparse matrix, we use *CSpMat* syntax, as shown in the last line of the example below.

```
public:


    int NumSite, TotalMatrixSize;
    vector<ElectronSite> ListOfSites;
    vector<OpenBoundaries> ListOfOpenBoundaries;
    CSpMat Hamiltonian, GR;
```

To set the size of yout sparse matrix the below command can be used :

```
this->Hamiltonian.resize(number of rows, number of columns);
```

To fill a sparse matrix like the Hamiltonian matrix of the system, we use a triplet vector. We use smaller blocks to fill the triplet vector, and then we turn the vector to a sparse matrix. In the below example, the *Filler* is a triplet vector. The *FillingTriplet* function is used to the *Filler*. We send the *Filler* as the first argument of the function. The second input argument is a small block that we want to put inside the Hamiltonian. The third and fourth arguments are the starting rows and columns in the Hamiltonian that we want to put the block. The last line is used to fill the Hamiltonian from the filler vector.

```
vector<TPT> Filler;

                  .
                  .
                  .

for (int j = 0; j < this->ListOfSites[i].
      ListOfTightBindingNeighbors.size(); j++)
{
     int J = ListOfSites[i].ListOfTightBindingNeighbors[j];
      FillingTriplet(Filler, this->ListOfSites[i]
          .ListOfOutwardsCouplingBlocks[j],
          I*OnSiteSize, J*OnSiteSize);
}

this->Hamiltonian.setFromTriplets(Filler.begin(),
                                  Filler.end());
```

A.1.5 Sanch algorithm

The decimal or Sancho algorithm is implemented to accelerate the surface Greens function calculation. This function can be found in "OpenBoundaries" class and has four input arguments. The first argument is the on-site Hamiltonian of one repeating unit cell of the lead (H_{00}). The second argument is the coupling matrix between two adjacent unit cells in the lead (H_{01}). The third and fourth arguments are the energy and broadening (η).

The *change_max* sets the value for convergence condition and after finishing the calculation, the surface Greens function is returned by the function.

```
// ************************************************** //
// ****************   Sancho Algorithm   **************** //
// ************************************************** //

CSpMat OpenBoundaries::Sancho(CSpMat& H00, CSpMat& H01, _cd energy,
                             _cd eta)
{
        int Size = this->F00.rows();

        CSpMat One(Size, Size);
        One.setIdentity();
```

```
CSpMat epsil, epsils, alpha, beta, alpha_0, beta_0, EH;
epsil = H00;
epsils = H00;
alpha = H01;
beta = H01.adjoint();
alpha_0 = alpha;
beta_0 = beta;

unsigned int counter = 0;
const unsigned int counter_max = 100;
_cd change_max = 2.5e-5;
double change = 1.0;
Complex E_New(energy, eta);

while (change > change_max && counter < counter_max)
{
        counter++;
        EH = E_New * One - epsil;
        CSpMat EH_New = SpInverse(EH);
        CSpMat alpha_New = alpha * EH_New * alpha;
        alpha = alpha_New;
        CSpMat beta_New = beta * EH_New * beta;
```

```
            beta = beta_New;
            CSpMat EpsilN = epsil + alpha_0 * EH_New * beta_0 +
                                    beta_0 * EH_New * alpha_0;
            epsil = EpsilN;
            CSpMat EpsilsN = epsils + alpha_0 * EH_New * beta_0;
            epsils = EpsilsN;

            change = (alpha - alpha_0).norm();
            alpha_0 = alpha;
            beta_0 = beta;
        }

        if (counter == counter_max)
            printf("Contact␣self␣energy␣didn't␣converge.\n");

        EH = E_New * One - epsils;

        CSpMat g =  SpInverse(EH);

        return g;
    }
```